

The Plerionic Supernova Remnant G21.5–0.9 Powered by PSR J1833–1034: New Spectroscopic and Imaging Results Revealed with the *Chandra* X-ray Observatory

Heather Matheson¹ and Samar Safi-Harb²

*Department of Physics and Astronomy, University of Manitoba,
Winnipeg, Manitoba, R3T 2N2, CANADA*

ABSTRACT

In 1999, the *Chandra* X-ray Observatory revealed a $150''$ -radius halo surrounding the $40''$ -radius pulsar wind nebula (PWN) G21.5–0.9. A 2005 imaging study of G21.5–0.9 showed that the halo is limb-brightened, and suggested this feature is a candidate for the long-sought supernova remnant (SNR) shell. We present a spectral analysis of SNR G21.5–0.9, using the longest effective observation to date (578.6 ks with the Advanced CCD Imaging Spectrometer (ACIS), 278.4 ks with the High-Resolution Camera (HRC)) to study unresolved questions about the spectral nature of remnant features, such as the limb-brightening of the X-ray halo and the bright knot in the northern part of the halo. The *Chandra* analysis favours the non-thermal interpretation of the limb. Its spectrum is well fit with a power-law model with a photon index $\Gamma = 2.13$ (1.94–2.33) and a luminosity of L_x (0.5–8 keV) = $(2.3 \pm 0.6) \times 10^{33}$ erg s^{−1} (at an assumed distance of 5.0 kpc). An *srcut* model was also used to fit the spectrum between the radio and X-ray energies. While the absence of a shell in the radio still prohibits constraining the spectrum at radio wavelengths, we assume a range of spectral indices to infer the 1 GHz flux density and the roll-off frequency of the synchrotron spectrum in X-rays, and find that the maximum energy to which electrons are accelerated at the shock ranges from ~ 60 –130 TeV $(B/10\mu\text{G})^{-1/2}$, where B is the magnetic field in units of μG . For the northern knot, we constrain previous models and find that a two-component power-law (or *srcut*) + *pshock* model provides an adequate fit,

¹matheson@physics.umanitoba.ca

²Canada Research Chair, samar@physics.umanitoba.ca

with the *pshock* model requiring a very low ionization timescale and solar abundances for Mg and Si. Our spectroscopic study of PSR J1833–1034, the highly energetic pulsar powering G21.5–0.9, shows that its spectrum is dominated by hard non-thermal X-ray emission with some evidence of a thermal component that represents $\sim 9\%$ of the observed non-thermal emission and that suggests non-standard rapid cooling of the neutron star. Finally, the ACIS and HRC-I images provide the first evidence for variability in the PWN, a property observed in other PWNe such as the Crab and Vela.

Subject headings: cosmic rays — ISM: individual (G21.5–0.9) — pulsars: individual (PSR J1833–1034) — stars: neutron — supernova remnants — X-rays: ISM

1. INTRODUCTION

A pulsar wind nebula (PWN, also ‘plerion’) is a filled-centre supernova remnant (SNR) which possesses a flat radio spectrum, centrally peaked radio and X-ray emission, highly polarized radio emission, and is powered by a rapidly rotating neutron star. G21.5–0.9 is a particularly interesting PWN since it was the first PWN discovered to be surrounded by an X-ray halo (Slane et al. 2000; Warwick et al. 2001; Safi-Harb et al. 2001) with limb-brightening (Matheson & Safi-Harb 2005; Bocchino et al. 2005).

In the 1970s, Becker & Kundu (1976) and Wilson & Weiler (1976) mapped G21.5–0.9 in the radio and found an elliptical brightness distribution with peak brightness near the geometric centre of the remnant, similar to the Crab Nebula. Fürst et al. (1988) performed 22.3 GHz observations and found axisymmetric filaments and suggested they resulted from a two-sided collimated outflow of particles in precession from a central pulsar. They also found that the X-ray maximum was located in a minimum in the small-scale radio emission, suggesting the two types of emission originate from the pulsar in a different way.

In 1999, *Chandra* revealed a $150''$ -radius halo at X-ray wavelengths surrounding the $40''$ -radius PWN (Slane et al. 2000; Safi-Harb et al. 2001). The spectrum of the PWN was well described by a power-law model with the photon index steepening (increasing) away from the central source. The X-ray halo was also detected with *XMM-Newton* and found to have a non-thermal spectrum that is consistent with the *Chandra* study (Warwick et al. 2001). The halo’s circular symmetry, lack of limb brightening, and non-thermal spectrum led to the earlier suggestion that the halo was an extension of the PWN rather than a shell formed by the blast wave of the supernova explosion. However, the lack of radio emission

from the halo would make this interpretation problematic as the size of the PWN in X-rays would then exceed the radio size by a factor of ~ 4 , a characteristic that is at odds with PWN morphology. Safi-Harb et al. (2001) noted that, since G21.5–0.9 is bright and heavily absorbed, a significant portion of the emitted X-rays could interact with dust and be scattered, forming a halo around the bright core. Bandiera & Bocchino (2004) modelled the halo as an effect of dust scattering in the foreground medium. While dust scattering could not explain the bright knots observed in the north of the remnant (referred to as the northern knot or ‘North Spur’, see Figure 1), a good fit can be obtained to the remainder of the halo. Matheson & Safi-Harb (2005) showed *Chandra* imaging results (modified version in Figure 1) revealing a candidate for the shell of the supernova remnant G21.5–0.9 in the form of limb-brightening at the eastern boundary of the X-ray halo. They also revealed previously unseen detail in the PWN, and showed that the power-law photon index increases from $\Gamma = 1.61 \pm 0.04$ (at the centre of the PWN) to $\Gamma = 2.15 \pm 0.13$ (at a radius of $40''$, the edge of the bright PWN), then remains flat at $\Gamma \sim 2.4$ inside the halo between a radius of $40''$ and $150''$ ($N_{\text{H}} = 2.2 \times 10^{22} \text{ cm}^{-2}$). Bocchino et al. (2005) used *XMM-Newton* and *Chandra* data to study the X-ray halo of G21.5–0.9. They interpret the diffuse halo as a dust scattering halo, the eastern limb as the location of particle acceleration at the forward shock, and the brightest northern knot (or ‘North Spur’) as a possible knot of ejecta in adiabatic expansion. However, the spectral nature of the northern knot and limb are still under debate. In particular, two solutions with different spectral properties were found for the northern knot. As well, the *Chandra* data used in Bocchino et al. (2005) had an effective exposure time that is ~ 2.5 times smaller than in our spectroscopic study presented here, prohibiting a clear detection of the limb-brightened feature. This will be addressed with our study presented here (see §3 and 5).

At higher energies, Bird et al. (2004) identified G21.5–0.9 in a soft γ -ray Galactic plane survey with *INTEGRAL*. The flux was measured to be $0.28 \pm 0.02 \text{ ct s}^{-1}$ in 20–40 keV and $0.26 \pm 0.03 \text{ ct s}^{-1}$ in 40–100 keV. De Rosa et al. (2009) detected G21.5–0.9 in the 17–200 keV range with *INTEGRAL*, showing that the main contribution to hard X-ray emission is from the PWN, with PSR J1833–1034 dominant above 200 keV. They also present *HESS* observations showing that PSR J1833–1034 is a bright gamma-ray emitter with a 1–10 TeV flux approximately 2% that of the Crab.

In the radio, Gupta et al. (2005) and Camilo et al. (2006) independently discovered the long sought pulsar (PSR J1833–1034) associated with G21.5–0.9. They found $P = 61.86 \text{ ms}$, $\dot{P} = 2.0 \times 10^{-13}$, a surface magnetic field of $B = 3.6 \times 10^{12} \text{ G}$, a characteristic age of 4.8 kyr, and a spin-down luminosity of $\dot{E} = 3.3 \times 10^{37} \text{ erg s}^{-1}$, making PSR J1833–1034 a highly energetic Galactic pulsar. Bietenholz & Bartel (2008), using VLA observations from 1991 and 2006, derived an expansion speed of $910 \pm 160 \text{ km s}^{-1}$ with respect to the centre of

the nebula and estimated the age of G21.5–0.9 as 870_{-150}^{+200} yr, making it one of the youngest known Galactic PWNe.

Camilo et al. (2006) used a compilation of studies to conclude that the best estimate of the distance to G21.5–0.9 was 4.7 ± 0.4 kpc. By comparing HI spectra with ^{13}CO emission spectra, Tian & Leahy (2008) also find a kinematic distance for G21.5–0.9 of ~ 4.8 kpc. In this paper we will adopt 5 kpc as the distance to G21.5–0.9.

Here we present a detailed spectroscopic analysis (Section 3) using the longest effective exposure time with *Chandra* to date (an extension of the preliminary study in Matheson & Safi-Harb (2005) which focused on imaging of G21.5–0.9) and discuss the open questions regarding the spectral nature of the northern knot and the limb-brightening to the east of the SNR. We also present the first evidence for thermal emission from the pulsar (Section 3.2) and for variability in the PWN (Section 4).

2. OBSERVATIONS

G21.5–0.9 was chosen as a calibration target for the *Chandra* X-ray Observatory and, as a result, G21.5–0.9 has been frequently observed using the Advanced CCD Imaging Spectrometer (ACIS) and the High Resolution Camera (HRC). Bocchino et al. (2005) made use of 21 *Chandra* observations (196.5 ks) to search for thermal emission from the northern knots of G21.5–0.9. However, multiple *Chandra* observations were combined into one dataset prior to extracting the spectra. The *Chandra* X-ray Center (CXC) recommends¹ generating spectra for each observation and analyzing them simultaneously, as we have done in the following analysis. We here made use of a larger set of 65 ACIS observations (1999 August – 2006 February, 578.6 ks, Table 1) in the variability study (§4). Since data observed at -100°C can not be corrected for charge transfer inefficiency (CTI), we made use of 56 ACIS observations (480.2 ks) in the spectroscopic analysis presented here, a factor of ~ 2.5 deeper than the study by Bocchino et al. (2005) and the deepest spectroscopic study to date. The variability study also made use of 15 HRC-I observations (1999 July – 2006 February, 278.4 ks, Table 1). For the imaging studies, observations were reprojected to align the images prior to merging. The data processing was performed using the CIAO² software package, and the

¹“The merged event list should not be used for spectral analysis, since it does not contain sufficient information to generate correct response files.” (<http://cxc.harvard.edu/ciao/threads/combine/>)

²Chandra Interactive Analysis of Observations (CIAO), <http://cxc.harvard.edu/ciao/>

spectral analysis was performed using *XSPEC*³.

2.1. Structure of G21.5–0.9

The combined *Chandra* image in Figure 1 shows the structure of G21.5–0.9. Located at $\alpha(2000) = 18^{\text{h}}33^{\text{m}}33^{\text{s}}.54$, $\delta(2000) = -10^{\circ}34'07''.6$ is a point source corresponding to the location of the pulsar PSR J1833–1034. The PWN is approximately $40''$ in radius and is seen to have indentations in the northwest and southeast. As well, many filamentary structures can be seen in the PWN. The X-ray halo extends to a radius of $153''$ with limb-brightening observed along the eastern edge. The foreground source SS 397 in the southwest portion of the halo was removed from the data prior to any spectral analysis. The northern portion of the halo is dominated by bright knots which appear to merge with the limb in the northeast. The brightest knot is located north and slightly to the west of the PWN. As mentioned earlier, this will be referred to as the ‘northern knot’ throughout the paper, and corresponds to the ‘North Spur’ studied by Bocchino et al. (2005). The open questions on these regions are studied further in Section 3.

Figure 2 zooms on the PWN and compares the *Chandra* data to radio data. Despite targeted searches for the SNR shell in the radio, the X-ray limb and halo have not yet been detected at radio wavelengths, except for the northern knot (Bietenholz et al. 2010). In Figure 2a, the contours from the X-ray image are overlaid on radio data taken with the Nobeyama Millimeter-Wave Array at 22.3 GHz (Fürst et al. 1988). Figure 2b combines the 0.2–10.0 ACIS X-ray data (blue) with the 22.3 GHz radio data (red) to show the similarity of the structure at both wavelengths. In Figure 2c, 4.75 GHz radio data from the VLA (see Bietenholz & Bartel (2008) for details) is coloured red and the 0.2–10.0 keV X-ray data is again coloured blue. The X-ray and radio structure are remarkably similar, with the radio following the shape of the X-ray PWN along the edges of the PWN, including indentations in the northwest and southeast. The PWN appears slightly larger at 4.75 GHz than at 22.3 GHz, but the images at 22.3 GHz and 0.2–10 keV are comparable in size, which indicates a small magnetic field in the PWN. Indeed, a low magnetic field estimate ($B \sim 25 \mu\text{Gauss}$, see also §5.2) has been inferred from modeling G21.5–0.9 (de Jager et al. 2008). The most prominent difference between the radio and X-ray emission is in the centre of the PWN. The pulsar is seen in a location that peaks in X-rays but has a minimum in radio emission. The X-ray emission traces the particles freshly injected by the pulsar, whereas the radio emission traces the older population characterized by a much larger synchrotron lifetime.

³X-ray Spectral Fitting Package (XSPEC), <http://xspec.gsfc.nasa.gov/>

The location of minimum radio emission could be indicative of a magnetic field direction along the line of sight, since the synchrotron emissivity scales as $\propto B_{\perp}^{\alpha+1}$ (where B_{\perp} is the magnetic field’s component that is perpendicular to the line of sight, and α is the spectral index). This interpretation is consistent with the radial magnetic field distribution inferred from polarization studies (Fürst et al. 1988).

3. SPECTROSCOPY

3.1. Spectra Creation

For each region shown in Figure 1, weighted spectra were extracted for every observation using the CIAO tools *dmcopy* and *dmextract*. The background chosen for each region is described in the section specific to that region.

To compensate for the effects of cosmic radiation damage, a charge transfer inefficiency (CTI) correction was applied to the ACIS data (CIAO CTI correction⁴ for ACIS-I, -120°C data, Penn State CTI correction⁵ (Townesley et al. 2000) for ACIS-I, -110°C and ACIS-S, -110°C and -120°C data). The -100°C data cannot be corrected for CTI and was therefore omitted from the spectral analysis.

For the observations that were CTI corrected using the Penn State CTI corrector, RMF files were provided with the corrector. For the observations that were CTI corrected with CIAO (*acis_process_events*), the tool *mkacisrmf* was used to create weighted RMF files.

The regions used in the following spectral analysis are listed in Table 2 and shown in Figure 1. The spectra were individually binned using the FTOOL⁶ *grppha* to improve the signal-to-noise ratio. The minimum number of counts per bin for the various regions are shown in Tables 3 and 4. All spectral models used contain a component which accounts for absorption along the line of sight (*wabs* in *XSPEC*). A power-law was used to model synchrotron emission from high energy electrons in a magnetic field. A blackbody model was used to study any thermal emission from the neutron star directly. A *pshock* model (a plane-parallel non-equilibrium ionization model with different ionization ages and a constant electron temperature, Borkowski et al. 2001) was used to search for thermal emission from shock-heated ejecta or interstellar matter. The *pshock* model is characterized by the

⁴<http://cxc.harvard.edu/ciao/why/cti.html>

⁵<http://www.astro.psu.edu/users/townsley/cti/>

⁶<http://heasarc.gsfc.nasa.gov/ftools/> (Blackburn 1995)

ionization timescale, $\tau = n_e t$, where n_e is the post-shock electron density and t is the time since the passage of the shock. The *vpshock* model is a *pshock* model which also accounts for variable abundances of metals. The *srcut* model was used to model the non-thermal component of the SNR associated with electrons accelerated by the SNR shock (see e.g. Reynolds & Keohane 1999). In order to use complete response information included with each observation, all spectra for a particular region were fit simultaneously. All errors are reported to the 90% confidence level.

3.2. PSR J1833–1034

Only observations with an off-axis angle less than $3'$ were used to study the compact source (Table 1). For an off-axis angle of $3'$, at 1.5 keV, 90% of the energy of a point source is contained within $1.5''$ (within $2.5''$ at 6.4 keV). Therefore a circular region with $2''$ radius, centered at $\alpha(2000) = 18^{\text{h}}33^{\text{m}}33^{\text{s}}.54$, $\delta(2000) = -10^{\circ}34'07''.6$, was defined as the extraction region for each dataset. The spectra were each grouped to have a minimum of 50 counts per bin and cover the energy range 0.5–8.0 keV. To remove contamination from the PWN, the background chosen was an annulus centred on PSR J1833–1034 with radius $2''$ – $4''$.

The best fit using an absorbed power-law model yields a column density of $N_{\text{H}} = 2.24^{+0.09}_{-0.10} \times 10^{22} \text{ cm}^{-2}$, a photon index of $\Gamma = 1.47^{+0.05}_{-0.06}$, and an observed flux in the 0.5–8.0 keV band of $(3.2 \pm 0.3) \times 10^{-12} \text{ erg cm}^{-2} \text{ s}^{-1}$ ($\chi^2 = 1287.9$ and $\nu = 1047$ degrees of freedom, see Table 3 for a list of parameters). This column density is consistent with previous work on G21.5–0.9 and with our global fit to the PWN, and will be used in the remainder of the spectral analysis. Fitting with an absorbed blackbody alone gives a low column density of $N_{\text{H}} = 0.78^{+0.05}_{-0.06} \times 10^{22} \text{ cm}^{-2}$ and a temperature of $kT_{\text{bb}} = 1.34^{+0.03}_{-0.03} \text{ keV} = 1.55^{+0.03}_{-0.03} \times 10^7 \text{ K}$ (reduced $\chi^2_{\nu} = 1.51$ and $\nu = 1047$). Freezing the column density to the acceptable value of $2.24 \times 10^{22} \text{ cm}^{-2}$ gives an unacceptable fit with a temperature of $kT_{\text{bb}} \sim 1.0 \text{ keV}$ and $\chi^2_{\nu} \sim 2.6$ for a single component blackbody. As expected, the blackbody fit alone is poor at low and high energies, indicating the need for a non-thermal component.

To test for a combination of thermal + magnetospheric emission, we freeze the hydrogen column density to $N_{\text{H}} = 2.24 \times 10^{22} \text{ cm}^{-2}$ and fit the pulsar’s emission with an absorbed *power-law+blackbody* model (Figure 3). The best fit ($\chi^2=1271.6$, $\nu=1046$) was obtained for a hard photon index of $\Gamma = 1.14^{+0.05}_{-0.07}$ and a temperature of $kT_{\text{bb}} = 0.52^{+0.03}_{-0.04} \text{ keV} = 6.0^{+0.3}_{-0.5} \times 10^6 \text{ K}$. This is an improved fit over the power-law fit alone, with an F-test probability of $\sim 2.6 \times 10^{-4}$. Additional observations of the pulsar will help confirm or constrain this emission.

The additional blackbody component suggests the first evidence for thermal emission

from the pulsar, a result that is observed in other young neutron stars. The observed thermal flux ($2.6 \pm 1.0 \times 10^{-13}$ erg cm $^{-2}$ s $^{-1}$) was found to be $\sim 9\%$ of the non-thermal flux ($3.0 \pm 0.6 \times 10^{-12}$ erg cm $^{-2}$ s $^{-1}$) in the 0.5–8.0 keV range. Converting the unabsorbed thermal flux ($7.4 \pm 3.0 \times 10^{-13}$ erg cm $^{-2}$ s $^{-1}$, $\sim 16\%$ of unabsorbed non-thermal flux) to luminosity, and assuming a blackbody, we can derive the size of the emitting area using the blackbody formula: $L = 4\pi R^2 \sigma T_{bb}^4 = 4\pi D^2 F$ (where σ is the Stephan-Boltzmann constant and F is the observed flux). The radius of the emitting region is found to be $R = 0.49 \pm 0.15$ km for a temperature of 0.52 keV. This is an unreasonably small radius for the size of a neutron star, suggesting that we may be instead be observing emission from a small “hot spot” on the surface of the neutron star. Detecting the X-ray pulsations is needed to confirm this interpretation⁷. Alternatively, constraining the radius of the emitting region to 12 km and assuming a distance of 5 kpc to G21.5–0.9, we use the *bbbodyrad* model to then calculate the surface temperature of the neutron star, assuming the thermal component is from the entire surface. In this case, the power-law model parameters are the same as those for the power-law model alone (with a photon index $\Gamma=1.47$) but we derive a lower temperature $kT = 0.11$ (<0.14) keV, corresponding to an effective temperature of 1.28 (<1.57) $\times 10^6$ K which is closer to what has been observed in other young neutron stars. This result is further discussed in §5.2.

3.3. X-ray Halo ($r = 45''$ – $153''$)

Since studying the emission from the limb requires subtracting the emission from the halo (to remove the contamination by the dust scattering halo), we here briefly summarize our spectral fit to the X-ray halo.

The X-ray halo of G21.5–0.9 is visible in Figure 1 at a radius of $45'' - 153''$ from the location of PSR J1833–1034. Since the northern half of the halo is dominated by emission from the knots, the southern half of the X-ray halo was selected for study. Emission from the eastern limb (defined between $125''$ and $153''$, see §3.4) and SS 397 was removed from the data prior to extracting the spectra. The background used was the southern half of an annulus with radius $153'' - 175''$. The halo was fit with a power-law with the column density fixed at the best fit value from PSR J1833–1034 ($N_H = 2.24^{+0.09}_{-0.10} \times 10^{22}$ cm $^{-2}$). We find a photon index of $\Gamma = 2.50^{+0.05}_{-0.05}$, $\chi^2_\nu = 1.08$, and $\nu = 865$ (Figure 4). The fit is improved by the addition of a thermal *pshock* component with a temperature of $kT = 0.33^{+0.12}_{-0.08}$ keV and

⁷Past searches for X-ray pulsations have only led to an upper limit on the pulsed fraction (Camilo et al. 2006, La Palombara & Mereghetti 2004, Safi-Harb et al. 2001)

an ionization timescale of $n_e t = 1.0^{+12.5}_{-1.0} \times 10^8 \text{ cm}^{-3} \text{ s}$ ($\Gamma = 2.25^{+0.11}_{-0.18}$, $\chi^2_\nu=1.04$, $\nu=862$). This fit to the halo is used in Section 3.4 to subtract the halo component from the limb region.

3.4. Eastern Limb (r = 125''–153'')

The eastern limb (Figure 1, radius = 125''–153''⁸) was studied to search for emission characteristic of a SNR shell. Due to the lower count rate in the limb, the background spectrum was extracted from a region outside the halo and therefore the data contains a component due to the halo. To correct for the halo emission we add a model component equal to the best fit to the halo (Section 3.3), with the normalization scaled to the area of the limb. The parameters for this component are all frozen and the fits presented below are emission from the limb only.

The *pshock* model was first used to search for thermal emission from interstellar matter shock-heated by the forward shock. As shown in Table 4, the *pshock* model provides an adequate fit ($\chi^2_\nu = 0.538$, $\nu = 909$); however with an unrealistically high temperature ($7.5^{+6.9}_{-2.5} \text{ keV}$), suggesting that the X-ray emission is likely non-thermal.

The limb of G21.5–0.9 can not be explained by a dust scattering halo nor by shock-heated ejecta (e.g. Bocchino et al. 2005) and must have another origin. Shocks in young supernova remnants have been known to accelerate electrons to TeV energies where they produce synchrotron X-rays (Reynolds 1998). To determine if the non-thermal component of the limb is due to this acceleration we used the *srcut* model in *XSPEC*. Since the limb has not yet been observed in the radio (Bietenholz et al. 2010), we do not know the radio spectral index (α , where $S \propto \nu^{-\alpha}$) for the limb and consider a range for α between 0.3 and 0.8, which covers the range observed for other supernova remnants (Green 2009). Similarly, without a radio observation of the shell, we do not know the 1 GHz radio flux density and so we leave it as a free parameter to find an estimate of the radio flux density. For $\alpha = 0.5$, which is typical for SNR shells, and $N_H = 2.24 \times 10^{22} \text{ cm}^{-2}$, we find a rolloff frequency of $\nu_{\text{rolloff}} = 4.3^{+9.2}_{-2.2} \times 10^{17} \text{ Hz}$, and a 1 GHz flux density of $4.9^{+0.7}_{-0.8} \times 10^{-3} \text{ Jy}$, corresponding to a surface brightness of $2.3^{+0.3}_{-0.4} \times 10^{-22} \text{ W m}^{-2} \text{ Hz}^{-1} \text{ sr}^{-1}$ for a solid angle $\Omega = 2.1 \times 10^{-7} \text{ sr}$ ($\chi^2_\nu = 0.541$, $\nu = 910$, Figure 5). This estimate of the surface brightness is a factor of ~ 17 times smaller than the upper limit obtained by Slane et al. (2000) and a factor of ~ 3 times smaller than the most recent upper limit of $7 \times 10^{-22} \text{ W m}^{-2} \text{ Hz}^{-1} \text{ sr}^{-1}$ obtained by Bietenholz et al. (2010) using a new sensitive 1.43-GHz observation with the Very Large

⁸Bocchino et al. (2005) chose a region between 115'' and 138'', with the outer radius located near the midpoint of the limb shown in our *Chandra* data.

Array (VLA).

For $\alpha = 0.3$ and $N_{\text{H}} = 2.24 \times 10^{22} \text{ cm}^{-2}$ with the model *srcut*, we find a rolloff frequency of $\nu_{\text{rolloff}} = 2.2_{-1.0}^{+2.5} \times 10^{17} \text{ Hz}$, and a 1 GHz flux density of $1.4_{-0.3}^{+0.2} \times 10^{-4} \text{ Jy}$, corresponding to a surface brightness of $6.7_{-1.4}^{+0.9} \times 10^{-24} \text{ W m}^{-2} \text{ Hz}^{-1} \text{ sr}^{-1}$ ($\chi_{\nu}^2 = 0.542$, $\nu = 910$), approximately two orders of magnitude smaller than the observed recent upper limit (Bietenholz et al. 2010). For $\alpha = 0.8$ and $N_{\text{H}} = 2.24 \times 10^{22} \text{ cm}^{-2}$ with the model *srcut*, we find a rolloff frequency of $\nu_{\text{rolloff}} = 8.7_{-3.3}^{+2400} \times 10^{17} \text{ Hz}$, and a 1 GHz flux density of $1.4_{-0.2}^{+0.3} \text{ Jy}$, corresponding to a surface brightness of $6.7_{-1.0}^{+1.4} \times 10^{-20} \text{ W m}^{-2} \text{ Hz}^{-1} \text{ sr}^{-1}$ ($\chi_{\nu}^2 = 0.542$, $\nu = 910$). This estimated surface brightness is two orders of magnitude higher than the recent upper limit by Bietenholz et al. (2010), suggesting the spectral index is at the lower end of the 0.3–0.8 range.

The quality of fit for each of the *power-law*, *pshock*, and *srcut* models are similar however the temperature for the thermal model is too high, confirming that the limb is dominated by non-thermal emission and strengthening the previous suggestion that it’s a possible site for cosmic ray acceleration (Bocchino et al. 2005, see §5). A two-component (thermal + non-thermal) model does not give well constrained parameters and so we have not included the results here.

3.5. Northern Knots

Bocchino et al. (2005) examined the brightest knot of emission to the north of the PWN (‘North Spur’). Using a two-component power-law plus thermal component (with the latter modelled by the *vnei* model, a non-equilibrium ionization model with a single ionization age and temperature, and with variable metal abundances), they found two solutions for the metal abundances with a similar quality of fit. The first solution is characterized by enhanced abundances for Mg and Si, with a Mg abundance of 0.6–3 times solar, a Si abundance of 2–20 times solar, a temperature of $kT \sim 0.17 \text{ keV}$, and an ionization timescale of $n_e t \sim 7 \times 10^{11} \text{ cm}^{-3} \text{ s}$. The second solution is characterized by solar abundances, a temperature of $kT \sim 0.30 \text{ keV}$, and a lower ionization timescale of $n_e t \sim 1 \times 10^{10} \text{ cm}^{-3} \text{ s}$. Here we explore the same region with more data in an attempt to better constrain the parameters.

Before attempting two-component models however, we first fit with single component models: a power-law or *srcut* model for a non-thermal interpretation and a *pshock*⁹ model

⁹we favour the *pshock* model over the *nei* model used by Bocchino et al. (2005) since the former includes a range of ionization timescales, which is more reasonable for an extended region like the northern knot.

for a thermal interpretation, and found the following. An absorbed power-law fit to the brightest knot in the north (Figure 1, background inside the halo) produces an artificially low hydrogen column density ($N_{\text{H}} = 0.98^{+0.15}_{-0.15} \times 10^{22} \text{ cm}^{-2}$) with $\chi^2_{\nu} = 0.98$ ($\nu = 605$). Freezing N_{H} to the best-fit value for PSR J1833–1034 ($2.24 \times 10^{22} \text{ cm}^{-2}$) gives a photon index of $\Gamma = 2.72^{+0.09}_{-0.09}$, an unabsorbed flux of $6.3 \times 10^{-13} \text{ erg cm}^{-2} \text{ s}^{-1}$, and an estimated X-ray luminosity (0.5–8.0 keV) of $1.9 \times 10^{33} \text{ erg s}^{-1}$ ($\chi^2_{\nu} = 1.18$, $\nu = 606$, assumed $D = 5 \text{ kpc}$) for the knot. While the fit is statistically acceptable, the residuals show evidence of line emission and the fit is improved by adding a thermal *pshock* component, as discussed below. Similarly, an *srcut* model alone is not favoured based on the evidence of thermal emission lines in the spectrum.

As shown in Table 4, the *pshock* model alone with a column density $N_{\text{H}} = 2.24 \times 10^{22} \text{ cm}^{-2}$ gives a temperature $kT = 4.9^{+0.9}_{-0.8} \text{ keV}$, and an ionization timescale $n_e t = 2.0^{+0.6}_{-0.4} \times 10^{10} \text{ cm}^{-3} \text{ s}$ with $\chi^2_{\nu} = 0.959$ ($\nu = 605$). Allowing the abundances of Mg, Si and S to vary we find that Mg = 1.08 (0.95–1.21), Si = 0.96 (0.79–1.13), and S = 0.52 (0.12–0.93); all consistent with solar abundances. While the fit is statistically acceptable, the shock temperature is unrealistically high, suggesting that the spectrum is dominated by non-thermal emission.

We therefore confirm the need for a two-component, thermal + non-thermal, model to fit the northern knot. As well we rule out an equilibrium ionization models (such as *MEKAL* used by Bocchino et al. 2005) for the thermal component, since the fit requires a low ionization timescale ($< 10^{12} \text{ cm}^{-3} \text{ s}$). Next, we explore the two solutions discussed in Bocchino et al. (2005).

Fitting a two-component model (*power-law+pshock*) to the northern knot ($N_{\text{H}} = 2.24 \times 10^{22} \text{ cm}^{-2}$), we find a photon index of $\Gamma = 2.21^{+0.15}_{-0.15}$, a temperature of $kT = 0.20^{+0.04}_{-0.06} \text{ keV}$, and an ionization timescale of $n_e t = 7.1^{+7.1}_{-3.4} \times 10^9 \text{ cm}^{-3} \text{ s}$ ($\chi^2_{\nu} = 0.96$, $\nu = 603$, Figure 6). The observed thermal flux is $(9.3 \pm 3.2) \times 10^{-15} \text{ erg cm}^{-2} \text{ s}^{-1}$, which is only $\sim 6\%$ that of the non-thermal flux $((1.6 \pm 0.3) \times 10^{-13} \text{ erg cm}^{-2} \text{ s}^{-1})$ in the 0.5–8.0 keV range, again confirming that the spectrum of the northern knot is dominated by non-thermal emission. Figures 7 and 8 show the range of values allowed by the above fit for the parameters of the *pshock* component. Figure 7 shows the relationship between kT and $n_e t$ and Figure 8 shows the relationship between the emission measure and $n_e t$. Allowing the abundances of Mg, Si and S to vary we find that Mg = 0.72 (0.40–1.06), Si = 0.84 (0.32–1.35), and S = 107.1 (3.9–210.3). Figure 9 shows that Mg and Si are consistent with solar, in agreement with solution 2 of Bocchino et al. (2005). We do not observe a solution with overabundances of Mg and Si, that is we rule out solution 1 of Bocchino et al. (2005). However we note that S (although poorly constrained) appears overabundant in our fits. While additional observations will help constrain the S abundance, we note that the apparent high S abundance might be an artifact of the

model used, because the S lies in the energy range where X-ray spectra from the *pshock* and power-law components overlap.

Finally, a two-component *srcut+pshock* model was used to further study the non-thermal emission from the northern knot that could be due to particle acceleration at a shock. We fix the column density, N_{H} , to $2.24 \times 10^{22} \text{ cm}^{-2}$ and the radio spectral index, α , to 0.5 (as for the limb, we also attempted other values for α in the range that brackets all possible spectral indices—see the results summarized in Table 4). We find a temperature of $kT = 0.21^{+0.04}_{-0.04} \text{ keV}$, an ionization timescale of $n_e t = 5.8^{+7.1}_{-1.8} \times 10^9 \text{ cm}^{-3} \text{ s}$, a rolloff frequency of $\nu_{\text{rolloff}} = 4.3^{+4.1}_{-2.1} \times 10^{18} \text{ Hz}$, and a 1 GHz flux density of $2.6^{+1.5}_{-0.9} \times 10^{-3} \text{ Jy}$ ($\chi^2_\nu = 0.963$, $\nu = 603$). The thermal flux ($1.0^{+1.5}_{-0.5} \times 10^{-14} \text{ erg cm}^{-2} \text{ s}^{-1}$) is again $\sim 7\%$ of the non-thermal flux ($1.5^{+0.9}_{-0.5} \times 10^{-13} \text{ erg cm}^{-2} \text{ s}^{-1}$) in the 0.5–8.0 keV range. Varying the abundances again yields Mg and Si abundances that are consistent with solar, but indicates enhanced (and poorly constrained) abundance for S; a result that is consistent with the power-law+*pshock* model above. We note that the derived 1 GHz flux density (for $\alpha=0.5$) is about an order of magnitude smaller than the flux density of $19 \pm 7 \text{ mJy}$ inferred from the radio detection of the northern knot with the VLA (Bietenholz et al. 2010). Freezing the *srcut* normalization to the measured value of $\sim 20 \text{ mJy}$ while fitting for the corresponding spectral index yields $\alpha = 0.61^{+0.03}_{-0.02}$, $kT = 0.21^{+0.03}_{-0.04} \text{ keV}$, $n_e t = 6.0^{+12.2}_{-2.6} \times 10^9 \text{ cm}^{-3} \text{ s}$, and a roll-off frequency $\nu_{\text{roll}} = 6.9^{+11.3}_{-3.7} \times 10^{17} \text{ Hz}$ ($\chi^2_\nu = 0.962$, $\nu = 603$). Due to the large uncertainty in the VLA spectral index measurement, our fitted value for α could not be excluded by the radio study and remains to be confirmed.

To conclude, the X-ray emission from the bright northern knot is dominated by non-thermal emission, suggesting cosmic ray acceleration at a shock. The thermal component does not require enhanced abundances of Mg and Si, suggesting that the second solution of Bocchino et al. (2005) is more reliable. The inferred low temperature, ionization timescale and solar abundances have been interpreted as evidence for possible interaction between ejecta and the H envelope of a type IIP SN.

4. VARIABILITY in the PWN

Variability has been previously observed in PWNe such as the Crab and Vela nebulae. The Crab nebula shows wisps (moving outward from the Crab pulsar with a velocity $\sim 0.5c$) and knots (that do not have the outward motion) which brighten quickly and fade over approximately one month (Hester et al. 2002). The Vela nebula has PWN features whose surface brightness changes up to $\sim 30\%$ and move with speeds up to $\sim 5000 \text{ km s}^{-1}$ (Pavlov et al. 2001). The Vela PWN also shows bright compact blobs moving at $0.3c$ – $0.6c$

which brighten and disappear over a couple of weeks (Pavlov et al. 2003). These remnants are located at approximately 40% and 10%, respectively, of the distance to G21.5–0.9, making changes in their morphology easier to detect than for G21.5–0.9.

Using the distance estimate of $D = 5$ kpc to G21.5–0.9, we estimate that features moving at a constant $0.5c$ would be expected to cover $\theta \sim 6.32'' \text{ yr}^{-1}$. Since the spatial resolution of *Chandra* is $\sim 0.5''$ and we have observations obtained over a period of 6 years, we can search for variability in G21.5–0.9.

Figures 10 (ACIS) and 11 (HRC-I) show the evolution of G21.5–0.9 over more than 6 years of *Chandra* observations (from 1999 Aug to 2006 Feb). These images are presented as movies in the online version of the journal. Observations with the same observing date were combined after reprojecting their coordinates to align the images, smoothed with a Gaussian of $\sigma = 1''$, and normalized to an effective exposure time of 20 ks. We can see knots that appear to change position between images. However, we have months between observations and previous observations of pulsar wind nebulae (Hester et al. 2002; Pavlov et al. 2003) have indicated that knots brighten and fade on a timescale of weeks. Therefore, we can not be sure that we are seeing the motion of knots rather than new knots that have appeared after the originals have faded.

Figure 12 shows HRC-I images of the PWN and demonstrates the high degree of variability in the nebula. We see that either there are knots in motion or old knots disappear and new knots appear between observations. Several clumps of emission are marked and we see that they either fade or move to a new location in the subsequent image. Assuming the knots persist, the knots labelled 6, 12, 13, and 14 can be located in the next image in the sequence and appear to have velocities $\sim 0.1c$ – $0.3c$. These knots are visible in the unsmoothed images, ensuring that the highlighted features are not an artifact of the smoothing.

Sample difference images created by subtracting one of the images in Figure 10 from the following image in the same sequence are presented in Figure 13. The emission near the pulsar was omitted to highlight the variability in the PWN. The background level in individual images was approximately 0.5 counts per pixel immediately surrounding the PWN. Ignoring regions in the range -0.5 to $+0.5$ counts per pixel, we see that white and red indicate regions that are brighter in the later image while black, purple, and blue indicate regions that are brighter in the earlier image. To the north of the pulsar location in Figure 13b we see a region of increased emission with a region of decreased emission to the west, spaced by $6.0''$. For a distance to G21.5–0.9 of 5 kpc, and assuming that we are observing the motion of a single knot, this corresponds to a knot velocity of $\sim 0.5c$.

The expansion of the nebula is not detectable in the observations presented here. This

may be due to the fact that the outer limit of the nebula ($\sim 40''$) is not well defined and there are wisps that appear and disappear. However, the expansion velocity of the PWN was estimated as $910 \pm 160 \text{ km s}^{-1}$ by Bietenholz & Bartel (2008). This velocity corresponds to an expansion of $0.038'' \pm 0.007''$ (less than 0.1 ACIS pixels) per year, suggesting the expansion of the PWN may not be detected with *Chandra* for several more years. In addition, the expansion of the shell is not detectable in this study, as a large number of observations are required to improve the signal-to-noise ratio so that the limb is more visible.

5. DISCUSSION

5.1. The SNR

The absence of shells around Crab-like SNRs has been a mystery for decades. Recent deep or targeted searches have been however in some cases successful in revealing the long sought SNR shells around PWNe. Aside from G21.5–0.9, shells have been found in 3C 58 (Gotthelf et al. 2007)¹⁰ and most recently G54.1+0.3 (Bocchino et al. 2010)¹¹. A shell has been unsuccessfully searched for around the Crab Nebula (Frail et al. 1995; Seward et al. 2006). A deep search with *Chandra* revealed a dust-scattered halo with an intensity of 5% that of the Crab, out to a radial distance of $18'$. However, there was no evidence of emission from shock-heated material in the form of a shell. The luminosities for the shells seen in 3C 58 and G21.5–0.9 are below the current upper limit of $L_X \sim 10^{34} \text{ erg s}^{-1}$ for the Crab Nebula (Seward et al. 2006)¹². The low luminosity of the shell in G21.5–0.9 ($\sim 2 \times 10^{33} \text{ erg s}^{-1}$ in the non-thermal interpretation) could be attributed to the fact that the SNR is young and expanding in a low-density medium, and so the shell may only now be coming into view. Furthermore, the heavy absorption towards G21.5–0.9 ($N_H = 2.2 \times 10^{22} \text{ cm}^{-2}$) explains the difficulty in detecting the SNR shell which became clearly visible (although only the eastern side) after accumulating $\sim 500 \text{ ksec}$ of *Chandra* time. Next, we will comment on the age of the SNR and the ambient density of the ISM in which it is expanding.

To estimate the density of the ISM in which the SNR is expanding, we use the *pshock*

¹⁰We note that the shell seen in 3C 58 has an extent that is smaller than the PWN, suggesting a shocked-ejecta origin, which is also strengthened by the evidence of enhanced abundances in the X-ray spectrum.

¹¹For G54.1+0.3, the presence of diffuse emission out to $\sim 10 \text{ pc}$ has been interpreted as evidence for the SNR shell. However, the available data did not yet reveal limb-brightening as expected from SNR shells.

¹²For G54.1+0.3, using the unabsorbed flux of $4.7 \times 10^{-12} \text{ erg cm}^{-2} \text{ s}^{-1}$ tabulated in Table 2 of Bocchino et al. (2010), we obtain a luminosity of $2.2 \times 10^{34} \text{ erg s}^{-1}$ at an assumed distance of 6.2 kpc.

fit to the limb¹³ which yields an emission measure of $EM = 3.7 \times 10^{-4} \text{ cm}^{-5}$. This implies that $\int n_e n_H dV \sim f n_e n_H V = 10^{14} (4\pi D^2) (EM) = 1.1 \times 10^{56} \text{ cm}^{-3}$ (assuming $D = 5 \text{ kpc}$), where f is the volume filling factor, n_e is the post-shock electron density, and $n_H \sim n_e/1.2$. Using a volume of $3.3 \times 10^{56} \text{ cm}^3$ (assuming the limb is a shell and the region we studied is $\sim 10\%$ of the shell volume), $n_e \sim 0.63 f^{-1/2} \text{ cm}^{-3}$, which implies an upstream ambient density $n_0 = n_e/4.8 = 0.13 f^{-1/2} \text{ cm}^{-3}$. For filling factors $f \sim 0.1 - 1.0$ this corresponds to $n_0 \sim 0.13 - 0.42 \text{ cm}^{-3}$ ($2.2 - 7.1 \times 10^{-25} \text{ g cm}^{-3}$ when n_0 includes only hydrogen). This estimate of the density is consistent with the upper limit of 0.65 cm^{-3} derived by Bocchino et al. (2005), and confirms that G21.5–0.9 is expanding into a low-density medium.

We subsequently comment on the non-thermal interpretation of the limb as evidence of cosmic ray acceleration to TeV energies. Young SNRs have been shown to accelerate cosmic rays to TeV energies at shock fronts (e.g. SN1006, Koyama et al. (1995)). The energy at which the electron energy distribution steepens from its slope at radio-emitting energies is given by

$$E_{\text{max}} = 10 \left(\frac{10\mu\text{G}}{B} \right)^{1/2} \left(\frac{\nu_{\text{rolloff}}}{0.5 \times 10^{16}} \right)^{1/2} \text{ TeV} \quad (1)$$

(Reynolds & Keohane 1999). Fitting the limb with the *srcut* model with a range $\alpha = 0.3 - 0.8$, we found that $\nu_{\text{rolloff}} \sim 2 - 9 \times 10^{17} \text{ Hz}$, which implies $E_{\text{max}} (B / (10\mu\text{G}))^{1/2} \sim 60 - 130 \text{ TeV}$. This range (60–130 TeV, for a magnetic field of $10\mu\text{G}$) implies that shells in plerionic SNRs could be important sites for cosmic ray acceleration to TeV energies. We note that the lower values of α give an upper limit on the maximum electron energy which is within the range of values found by Reynolds & Keohane (1999) for young shell-type supernova remnants. The predicted E_{max} is dependent on ν_{rolloff} , which is very dependent on α that remains to be measured in the radio. The magnetic field estimate in the region surrounding the limb is also needed to refine the estimated maximum energies for the accelerated particles.

Finally, we note that the non-thermal component of the northern knot also implies cosmic ray acceleration at a shock—possibly resulting from the interaction between ejecta and the H envelope of a type IIP SN (see §3.5). Using the *srcut* model component with $\alpha=0.6$ (the likely value based on its radio detection, see §3.5), the derived roll-off frequency is $\nu_{\text{roll}} = 6.9 (3.2 - 18.2) \times 10^{17} \text{ Hz}$, which yields $E_{\text{max}} = 117 (80 - 191) \text{ TeV}$ (again assuming $B = 10\mu\text{G}$).

¹³Since we believe the X-ray spectrum of the limb is dominated by non-thermal emission, the derived estimate of the ambient density should be only viewed as an upper limit.

5.2. The PWN and pulsar

Camilo et al. (2006) show that inside the elliptical emission region containing the pulsar, the compact source is offset to the northeast from the centre of the ellipse. The HRC-I image shown in Figure 14 confirms this offset. The image is centred on PSR J1833–1034, smoothed by 2 pixels ($0.2635''$), and is $9'' \times 9''$. Using the ACIS imaging data used to produce Figure 1, we measured the distance between the location of the pulsar and the centre of the arc traced by the eastern limb. PSR J1833–1034 is found to be offset from the centre of the shell of G21.5–0.9 by $7.5''$, which is equivalent to a 0.18 pc offset for a distance to G21.5–0.9 of 5 kpc. For a remnant age of 870_{-150}^{+200} , this corresponds to a 2-D pulsar velocity of 200 ± 40 km s $^{-1}$. This velocity is comparable with the average 2-D speed of 246 ± 22 km s $^{-1}$ derived for ‘normal’ pulsars by Hobbs et al. (2005).

The PWN of G21.5–0.9 demonstrates the type of variability previously observed in other PWNe, including bright knots which appear, move at speeds of $\sim 0.1c$ – $0.3c$, and fade with time. There is no evidence of expansion of the nebula, nor do we expect to observe any with this sequence of observations (§4).

Using $B_{eq} \sim 0.3$ mG and $\dot{E} = 3.37 \times 10^{37}$ erg s $^{-1}$ for G21.5–0.9, Camilo et al. (2006) calculate the characteristic scale of the wind termination shock around PSR J1833–1034 to be $\sim 1''.6$, which corresponds to $r_t = 1.2 \times 10^{17}$ cm = 0.04 pc for a distance of 5 kpc to G21.5–0.9 (Section 1). For an off-axis angle of $3'$, at 1.5 keV, 90% of the encircled energy of a point source is contained within $2.5''$ (within $1.5''$ at 6.4 keV) with ACIS. For the HRC data, the 90% encircled energy radius is $0.9''$ at 1.5 keV and $2.0''$ at 6.4 keV (for an off-axis angle of $0.3''$). The estimated termination shock radius is then comparable to the point-spread function, making it difficult to distinguish the termination shock from the pulsar emission. Recent estimates of the magnetic field strength in the nebula predict a field strength which is an order of magnitude below equipartition. de Jager et al. (2008) estimate the current field strength as 25 μ G and Tanaka & Takahara (2010) estimate 64 μ G.

In Section 3.2 we presented the spectroscopic analysis of PSR J1833–1034, the pulsar powering G21.5–0.9. The X-ray spectrum is dominated by hard non-thermal emission, with evidence of a thermal blackbody component that represents $\sim 9\%$ of the non-thermal flux observed from the pulsar in the 0.5 – 8.0 keV range. While this additional component needs to be confirmed/constrained with additional observations of the pulsar, we comment next on the implication of this detection. Tsuruta et al. (2002) used X-ray observations of neutron stars to compare NS cooling theories. They found that less massive stars appear to cool by standard cooling (conventional slower neutrino cooling mechanisms: modified Urca, plasmon neutrino, bremsstrahlung) while more massive stars cool by non-standard cooling (exotic, extremely fast cooling processes: direct Urca processes involving nucleons, hyperons,

pions, kaons, & quarks). For an age of 870^{+200}_{-150} years (Bietenholz & Bartel 2008) and a luminosity of $L_{\infty} \sim 1.3^{+0.5}_{-0.5} \times 10^{33}$ erg s $^{-1}$ (*blackbody* component of the *power-law+blackbody* fit, see Section 3.2), PSR J1833–1034 falls between the non-standard and standard cooling curves. It is however closer to the non-standard curve than the standard curve, which imply luminosities of $L_{\infty} \sim 5 \times 10^{32}$ erg s $^{-1}$ and $\sim 9 \times 10^{33}$ erg s $^{-1}$, respectively, for a 870 year-old neutron star. Fixing the radius to 12 km, the luminosity of the *bbbodyrad* component is $\sim 5.9 \times 10^{32}$ erg s $^{-1}$, consistent with the non-standard cooling curve of Tsuruta et al. (2002). Other young neutron stars observed to have thermal components in their spectra also point to rapid cooling by non-standard processes (Slane et al. 2004). The blackbody fit presented here for PSR J1833–1034 yields a temperature that is higher or comparable to that inferred for other young pulsars ($T_{\infty} \sim 5 \times 10^6$ K, reduced to $\sim 1 \times 10^6$ K when fixing the size of the emitting region to that of the neutron star surface). For example, PSR J0205+6449 (~ 830 year-old based on its probable association with SN 1181) in 3C 58 has an upper limit on its temperature of 1.02×10^6 K (Slane et al. 2004), while the highly magnetized and young pulsar PSR J1119-6127 (with a characteristic age of ~ 1600 years) in G292.2–0.5 has a temperature of $(1.2\text{--}2.5) \times 10^6$ K (Safi-Harb & Kumar 2008).

6. CONCLUSIONS

We have made use of 6 years of archival *Chandra* data to demonstrate the importance of deep searches for shells surrounding plerionic supernova remnants. The technology incorporated into *Chandra* made it possible to study the SNR G21.5–0.9 in detail at a high spatial and spectral resolution by combining many short observations into one effective exposure of 578.6 ks with ACIS and one of 278.4 ks with HRC.

The spectroscopic analysis presented here extends the study by Matheson & Safi-Harb (2005). The *Chandra* data clearly reveal a partial shell on the eastern side of the SNR, suggesting the detection of the long sought SNR shell. This (partial) shell surrounding the PWN has a radius of ~ 3.6 pc and is centred $7.5''$ from PSR J1833–1034. Its spectrum is equally well fit by thermal (*pshock*) and non-thermal models (power-law or *srcut*—a curved model with a cutoff in the relativistic electron distribution). However, the thermal model gives an unreasonably high temperature, indicating that the non-thermal interpretation is more physical. While a two-component model can not be ruled out, the quality of the data is not sufficient to reliably fit the spectrum of the limb. In the non-thermal interpretation, the shell has a luminosity of $\sim 2\text{--}3 \times 10^{33}$ erg s $^{-1}$ and may be the site of cosmic ray acceleration up to $\sim 60\text{--}130$ TeV energies (for a magnetic field of $10\mu\text{G}$). The derived upper limit for the upstream density is $\sim 0.1\text{--}0.4$ cm $^{-3}$, confirming that G21.5–0.9 is expanding in a rarefied

medium. Additional X-ray observations of G21.5–0.9 will help better constrain any thermal emission from the limb and may potentially detect the western side of the shell.

In addition, we addressed the spectral nature of the northern knot (also known as North Spur studied by Bocchino et al. 2005) detected in the X-ray halo between the PWN and the outer limb. We confirm that its spectrum is best fit with a combination of non-thermal and thermal components; however with the thermal component characterized by a low ionization timescale and solar abundances for Mg and Si. This favours the interpretation of the northern knot resulting from interaction between ejecta and the H envelope of a type IIP SN. Furthermore, the non-thermal component of the emission from the knot could be well fit with the *srcut* model, characterized by a roll-off frequency of $6.9^{+11.3}_{-3.7} \times 10^{17}$ Hz for a radio spectral index $\alpha=0.6$. Constraining the spectral index of the knot, detected with the VLA, is needed to confirm this result.

Our spectroscopic study of the powering engine of G21.5–0.9, the highly energetic 61.86 ms pulsar PSR J1833–1034, showed that its X-ray spectrum is dominated by non-thermal emission, with evidence for thermal X-ray emission from the neutron star. The observed thermal component, yet to be confirmed with additional spectroscopic and timing observations of the pulsar, represents $\sim 9\%$ the non-thermal emission and suggests non-standard rapid cooling of the neutron star.

Finally, the *Chandra* data also allowed us to demonstrate for the first time the variable nature of the PWN, identifying knots that appear and disappear with time. However, due to the time between observations we can not be sure we are observing one knot over time rather than a new one that has appeared after the original faded.

Thanks to Roland Kothes for providing the 22.3 GHz radio data used in Figure 2. Thanks also to Michael Bietenholz for providing the 4.75 GHz VLA map of the PWN shown in Figure 2, and for comments on the manuscript. We thank the referee for comments on the manuscript. H.M. acknowledges the support of the Natural Sciences and Engineering Research Council of Canada (NSERC) in the form of a Canada Graduate Scholarship and the support of the Province of Manitoba in the form of a Manitoba Graduate Scholarship. S.S.H. is supported by an NSERC Discovery Grant and the Canada Research Chairs program.

REFERENCES

- Bandiera, R., & Bocchino, F. 2004, *AdSpRes*, 33, 398
- Becker, R.H., & Kundu, M.R. 1976, *ApJ*, 204, 427
- Bietenholz, M.F., & Bartel, N. 2008, *MNRAS*, 386, 1411
- Bietenholz, M.F., Matheson, H., Safi-Harb, S., Brogan, C., & Bartel, N. 2010, submitted to *MNRAS*
- Bird, A.J., et al. 2004, *ApJ*, 607, L33
- Blackburn, J.K. 1995, *ASP Conf. Ser.*, 77, 367
- Bocchino, F., van der Swaluw, E., Chevalier, R., & Bandiera, R. 2005, *A&A*, 442, 539
- Bocchino, F., Bandiera, R. & Gelfand, J. 2010, preprint (arXiv:1004.3515v1)
- Borkowski, K., Lyerly, W. J., Reynolds, S. P. 2001, *ApJ*, 548, 820
- Camilo, F., Ransom, S.M., Gaensler, B.M., Slane, P.O., Lorimer, D.R., Reynolds, J., Manchester, R.N., & Murray, S.S. 2006, *ApJ*, 637, 456
- de Jager, O.C., Ferreira, S.E.S., & Djannati-Ataï, A. 2008, in *High Energy Gamma-Ray Astronomy, 4th International Meeting on High Energy Gamma-Ray Astronomy*, ed. F.A. Aharonian, W. Hofmann, & F.M. Rieger (AIPC), 199
- de Rosa, A., Ubertini, P., Campana, R., Bazzano, A., Dean, A.J., & Bassani, L. 2009, *MNRAS*, 393, 527
- Frail, D.A., Kassim, N.E., Cornwell, T.J., & Goss, W.M. 1995, *ApJ*, 454, L129
- Fürst, E., Handa, T., Morita, K., Reich, P., Reich, W., Sofue, Y. 1988, *Publ. Astron. Soc. Japan*, 40, 347
- Gotthelf, E.V., Helfand, D.J., & Newburgh, L. 2007, *ApJ*, 654, 267
- Green, D.A. 2009, *BASI*, 37, 45.
- Gupta, Y., Mitra, D., Green, D.A., & Acharyya, A. 2005, *Current Science*, 89
- Hester, J.J., et al. 2002, *ApJ*, 577, L49
- Hobbs, G., Lorimer, D.R., Lyne, A.G., & Kramer, M. 2005, *MNRAS*, 360, 974

- Koyama, K., Petre, R., Gotthelf, E.V., Hwang, U., Matsuura, M., Ozaki, M., & Holt, S.S. 1995, *Nature*, 378, 255
- La Palombara, N. & Mereghetti, S. 2002, *A&A*, 383, 916
- Matheson, H., & Safi-Harb, S. 2005, *AdSpRes*, 35, 1099
- Pavlov, G.G., Kargaltsev, O.Y., Sanwal, D., & Garmire, G.P. 2001, *ApJ*, 554, L189
- Pavlov, G.G., Teter, M.A., Kargaltsev, O., & Sanwal, D. 2003, *ApJ*, 591, 1157
- Reynolds, S.P. 1998, *ApJ*, 493, 375
- Reynolds, S.P., & Keohane, J.W. 1999, *ApJ*, 525, 368
- Safi-Harb, S., Harrus, I.M., Petre, R., Pavlov, G.G., Koptsevich, A.B., & Sanwal, D. 2001, *ApJ*, 561, 308
- Safi-Harb, S., & Kumar, H.S. 2008, *ApJ*, 684, 532
- Seward, F.D., Gorenstein, P., & Smith, R.K. 2006, *ApJ*, 636, 873
- Slane, P., Chen, Y., Schulz, N.S., Seward, F.D., Hughes, J.P., & Gaensler, B.M. 2000, *ApJ*, 533, L29
- Slane, P., Helfand, D.J., van der Swaluw, E., & Murray, S.S. 2004, *ApJ*, 616, 403
- Tanaka, S.J. & Takahara, F. 2010, private communication
- Tian, W. W. & Leahy, D. A. 2008, *MNRAS*, 391, L54
- Townsley, L.K., Broos, P.S., Garmire, G.P., & Nousek, J.A. 2000, *ApJ*, 534, L139
- Tsuruta, S., Teter, M.A., Takatsuka, T., Tatsumi, T., & Tamagaki, R. 2002, *ApJ*, 571, L143
- Warwick, R.S., et al. 2001, *A&A*, 365, L248
- Wilson, A.S., & Weiler, K.W. 1976, *A&A*, 53, 89

Table 1. Net exposure times and off-axis angles for *Chandra* data

Detector	Time (ks)	Observations (observation date, off-axis angle (arcmin))
ACIS-I, -100°C	41.9	158 (1999 Aug 25, 5.8), 160 (1999 Aug 25, 6.7), 161 (1999 Aug 25, 5.9), 162 (1999 Aug 27, 1.7)
ACIS-I, -110°C	100.4	1233 (1999 Nov 5, 1.7), 1441 (1999 Nov 15, 9.3), 1442 (1999 Nov 15, 5.8), 1443 (1999 Nov 15, 5.9), 1772 (2000 Jul 5, 7.3), 1773 (2000 Jul 5, 5.8), 1774 (2000 Jul 5, 4.3), 1775 (2000 Jul 5, 2.5), 1776 (2000 Jul 6, 0.8), 1777 (2000 Jul 6, 5.8), 1778 (2000 Jul 6, 4.3), 1779 (2000 Jul 6, 2.5)
ACIS-I, -120°C	156.5	1551 (2001 Mar 8, 2.5), 1552 (2001 Jul 13, 2.5), 1719 (2000 May 23, 7.3), 1720 (2000 May 23, 5.8), 1721 (2000 May 23, 4.3), 1722 (2000 May 23, 2.5), 1723 (2000 May 23, 0.8), 1724 (2000 May 24, 5.8), 1725 (2000 May 24, 4.3), 1726 (2000 May 24, 2.5), 2872 (2002 Sep 13, 3.7), 3473 (2002 May 16, 7.0), 3692 (2003 May 16, 2.5), 3699 (2003 Nov 9, 3.7), 5158 (2005 Feb 26, 3.8), 5165 (2004 Mar 26, 3.8), 6070 (2005 Feb 26, 3.8), 6740 (2006 Feb 21, 3.8)
ACIS-S, -100°C	36.8	159 (1999 Aug 23, 0.3), 165 (1999 Aug 23, 6.2), 1230 (1999 Aug 23, 0.3)
ACIS-S, -110°C	68.2	1433 (1999 Nov 15, 1.2), 1434 (1999 Nov 16, 6.2), 1769 (2000 Jul 5, 1.3), 1770 (2000 Jul 5, 1.3), 1771 (2000 Jul 5, 1.3), 1780 (2000 Jul 5, 4.7), 1781 (2000 Jul 5, 4.7), 1782 (2000 Jul 5, 4.7)
ACIS-S, -120°C	174.8	1553 (2001 Mar 18, 1.3), 1554 (2001 Jul 21, 1.2), 1716 (2000 May 23, 1.3), 1717 (2000 May 23, 1.3), 1718 (2000 May 23, 1.3), 1727 (2000 May 24, 4.7), 1728 (2000 May 24, 4.6), 1729 (2000 May 24, 4.6), 1838 (2000 Sep 2, 1.2), 1839 (2000 Sep 2, 2.4), 1840 (2000 Sep 2, 5.3), 2873 (2002 Sep 14, 1.2), 3474 (2002 May 16, 7.0), 3693 (2003 May 16, 1.2), 3700 (2003 Nov 9, 1.2), 4353 (2003 May 15, 5.2), 5159 (2004 Oct 27, 1.2), 5166 (2004 Mar 14, 1.2), 6071 (2005 Feb 26, 1.3), 6741 (2006 Feb 22, 1.3)
HRC-I	278.4	142 (2000 Feb 16, 0.3), 143 (1999 Sep 4, 0.3), 144 (2000 Sep 1, 0.3), 1242 (1999 Sep 4, 0.4), 1298 (1999 Sep 4, 0.3), 1406 (1999 Oct 25, 0.3), 1555 (2001 Mar 9, 0.3), 1556 (2001 Jul 13, 0.3), 2867 (2002 Mar 13, 0.3), 2874 (2002 Jul 15, 0.3), 3694 (2003 May 15, 0.3), 3701 (2003 Nov 9, 0.2), 5167 (2004 Mar 25, 0.3), 6072 (2005 Feb 26, 0.3), 6742 (2006 Feb 21, 0.3)

Table 2. The regions studied in G21.5–0.9 (see Fig. 1)

Region	Background Subtracted Count Rate ^a (cts/s)	Total Exposure Time (ks)	Area (arcmin ²)
PSR J1833–1034	0.175 ± 0.024	238.9	0.0035
Southern Halo	$(1.14 \pm 0.19) \times 10^{-1}$	255.6	6.481
Brightest Knot	$(1.44 \pm 0.24) \times 10^{-2}$	360.6	0.073
Eastern Limb	$(5.03 \pm 0.85) \times 10^{-2}$	315.6	2.260

^ain the energy range 0.5–8.0 keV

Table 3. Spectral fitting results for PSR J1833–1034^a.

Compact Source		
min # cts/bin	50	
power-law	N_H (10^{22} atoms cm ⁻²)	2.24 (2.14 - 2.33)
	Γ	1.47 (1.41 - 1.52)
	norm (10^{-4}) ^b	7.73 (7.11 - 8.40)
	χ^2_ν (ν)	1.230 (1047)
	flux (10^{-12}) ^c	3.2 ± 0.3
	luminosity (10^{34} erg s ⁻¹)	1.63 ± 0.14
power-law + blackbody	N_H (10^{22} atoms cm ⁻²)	2.24 (frozen)
	Γ	1.14 (1.07 - 1.19)
	norm (10^{-4}) ^b	4.45 (3.59 - 5.26)
	kT (keV)	0.52 (0.48 - 0.55)
	norm (10^{-6}) ^d	9.06 (5.42 - 12.48)
	χ^2_ν (ν)	1.216 (1046)
	flux (10^{-12}) ^c	3.3 ± 0.7
	luminosity (10^{34} erg s ⁻¹)	1.6 ± 0.4
	thermal flux (10^{-13}) ^c	2.6 ± 1.1
	non-thermal flux (10^{-12}) ^c	3.0 ± 0.6

^aAll confidence ranges are 90%. All models were fit to the data in the range 0.5–8.0 keV. The values given for luminosity assume a distance of 5 kpc to G21.5–0.9.

^bUnits for the normalization factor on the power-law model are photons keV⁻¹ cm⁻² s⁻¹.

^cObserved flux in units of erg cm⁻² s⁻¹.

^dThe normalization factor on the blackbody model is L_{39}/D_{10}^2 where $L_{39}=L/(10^{39}$ erg s⁻¹) and $D_{10}=D/(10$ kpc).

Table 4. Spectral fitting results for the X-ray halo of G21.5–0.9^a.

		Southern Halo	Brightest Northern Knot	Eastern Limb
min # cts/bin		50	10	20
power-law	Γ	2.50 (2.45 - 2.54)	2.72 (2.63 - 2.80)	2.13 (1.94 - 2.33)
	norm (10^{-4}) ^b	14.4 (13.7 - 15.1)	1.99 (1.82 - 2.17)	1.8 (1.4 - 2.3)
	χ^2_ν (ν)	1.08 (865)	1.18 (606)	0.539 (910)
	flux (10^{-13}) ^c	14.2 ± 0.7	1.5 ± 0.2	3.0 ± 0.7
	luminosity (10^{33} erg s ⁻¹)	14.6 ± 0.7	1.9 ± 0.2	2.3 ± 0.6
pshock	kT keV	3.83 (3.62 - 4.10)	4.89 (4.18 - 5.99)	7.5 (5.0 - 14.4)
	$n_e t$ (10^9 cm ⁻³ s)	6.8 (6.2 - 7.4)	20.1 (16.5 - 25.8)	8.7 (5.6 - 13.2)
	norm (10^{-3} cm ⁻⁴)	2.51 (2.39 - 2.63)	0.22 (0.19 - 0.24)	3.7 (3.0 - 4.4)
	χ^2_ν (ν)	1.30 (864)	0.959 (605)	0.538 (909)
	flux (10^{-12}) ^c	1.4 ± 0.1	0.17 ± 0.02	0.32 ± 0.06
	luminosity (10^{34} erg s ⁻¹)	8.8 ± 0.7	0.83 ± 0.09	1.3 ± 0.3
	Mg		1.08 (0.95 - 1.21)	0.83 (0.22 - 1.44)
	Si		0.96 (0.79 - 1.13)	0.86 (0.25 - 1.47)
	S		0.52 (0.12 - 0.93)	0.94 (0 - 2.48)
power-law + pshock	Γ	2.25 (2.08 - 2.36)	2.21 (2.06 - 2.36)	
	norm (10^{-4}) ^b	10.4 (9.0 - 12.1)	1.08 (0.89 - 1.31)	
	kT keV	0.33 (0.25 - 0.45)	0.20 (0.14 - 0.24)	
	$n_e t$ (10^9 cm ⁻³ s)	0.1 (< 1.3)	7.1 (3.7 - 14.2)	
	norm (10^{-2} cm ⁻²)	2.6 (1.1 - 7.3)	5.2 (3.4 - 21.4)	
	χ^2_ν (ν)	1.04 (862)	0.960 (603)	
	flux (10^{-13}) ^c	15 ± 3	1.7 ± 0.4	
	luminosity (10^{35} erg s ⁻¹)	0.19 (0.13 - 0.34)	1.6 ± 1.5	
	non-thermal flux (10^{-13}) ^c	14 ± 2	1.6 ± 0.3	
	thermal flux (10^{-15}) ^c	46 (19 - 129)	9.3 ± 3.2	
	Mg		0.73 (0.40 - 1.06)	
	Si		0.84 (0.32 - 1.35)	
	S		107.1 (3.9 - 210.3)	
srcut	α	0.5 (frozen)	0.5 (frozen)	0.3 (frozen) / 0.5 (frozen) / 0.8 (frozen)
	ν_{rolloff} (10^{17} Hz)	1.26 (1.11 - 1.42)	0.72 (0.60 - 0.93)	2.2 (1.2 - 4.7) / 4.3 (2.1 - 13.5) / 8.7 (5.4 - 2400)
	norm (10^{-2} Jy)	7.1 (6.9 - 7.3)	1.47 (1.40 - 1.54)	0.014 (0.011 - 0.016) / 0.49 (0.41 - 0.56) / 140 (120 - 170)
	χ^2_ν (ν)	1.14 (865)	1.24	0.542 (910) / 0.541 (910) / 0.542 (910)
	flux (10^{-13}) ^c	13.8 ± 0.5	1.5 ± 0.5	2.9 ± 0.5 / 2.9 ± 0.4 / 2.7 ± 0.5
	luminosity (10^{33} erg s ⁻¹)	12.9 ± 0.5	1.6 ± 0.7	2.0 ± 0.3 / 2.1 ± 0.3 / 2.2 ± 0.4
srcut + pshock	α	0.5 (frozen)	0.3 (frozen) / 0.5 (frozen) / 0.8 (frozen)	
	ν_{rolloff} (10^{17} Hz)	4.2 (2.9 - 8.7)	2.2 (1.4 - 3.1) / 4.3 (2.4 - 8.4) / 18 (8 - 65)	
	norm (10^{-3} Jy)	24.2 (23.4 - 25.0)	0.074 (0.048 - 0.117) / 2.6 (1.7 - 4.1) / 580 (380 - 850)	
	kT keV	0.38 (0.33 - 0.43)	0.21 (0.18 - 0.25) / 0.21 (0.17 - 0.25) / 0.20 (0.16 - 0.24)	
	$n_e t$ (10^9 cm ⁻³ s)	0.1 (< 0.98)	5.6 (3.3 - 13.2) / 5.8 (4.0 - 12.9) / 6.3 (3.4 - 24.8)	
	norm (10^{-2} cm ⁻⁵)	2.2 (1.3 - 2.9)	3.9 (2.1 - 8.7) / 4.1 (2.1 - 9.6) / 4.6 (2.2 - 10.8)	
	χ^2_ν (ν)	1.04 (862)	0.963 (603) / 0.963 (603) / 0.962 (603)	
	flux (10^{-13}) ^c	14.7 ± 0.8	1.6 ± 0.9 / 1.6 ± 0.6 / 1.6 ± 0.9	
	luminosity (10^{34} erg s ⁻¹)	1.8 ± 0.3	13.6 ± 5.9 / 14.0 ± 7 / 15.0 ± 7.7	
	non-thermal flux (10^{-13}) ^c	13.9 ± 0.5	1.5 ± 0.9 / 1.5 ± 0.5 / 1.5 ± 0.9	
	thermal flux (10^{-14}) ^c	7.3 (4.3 - 9.8)	1.1 ± 0.5 / 1.0 ± 0.5 / 1.0 ± 0.7	
	Mg		0.74 (0.41 - 1.07) / 0.74 (0.41 - 1.07) / 0.73 (0.40 - 1.06)	
	Si		0.84 (0.35 - 1.33) / 0.84 (0.34 - 1.34) / 0.84 (0.34 - 1.35)	
	S		96.7 (10.3 - 183.1) / 98.9 (9.0 - 188.7) / 102.6 (5.9 - 199.3)	

^aThe column density N_{H} was fixed at $2.24 \times 10^{22} \text{ cm}^{-2}$, the best fit value obtained from the pulsar. All confidence ranges are 90%. All models were fit to the data in the range 0.5–8.0 keV. The values given for luminosity assume a distance of 5 kpc to G21.5–0.9.

^bUnits for the normalization factor on the power-law model are $\text{photons keV}^{-1} \text{ cm}^{-2} \text{ s}^{-1}$.

^cObserved flux in $\text{erg cm}^{-2} \text{ s}^{-1}$.

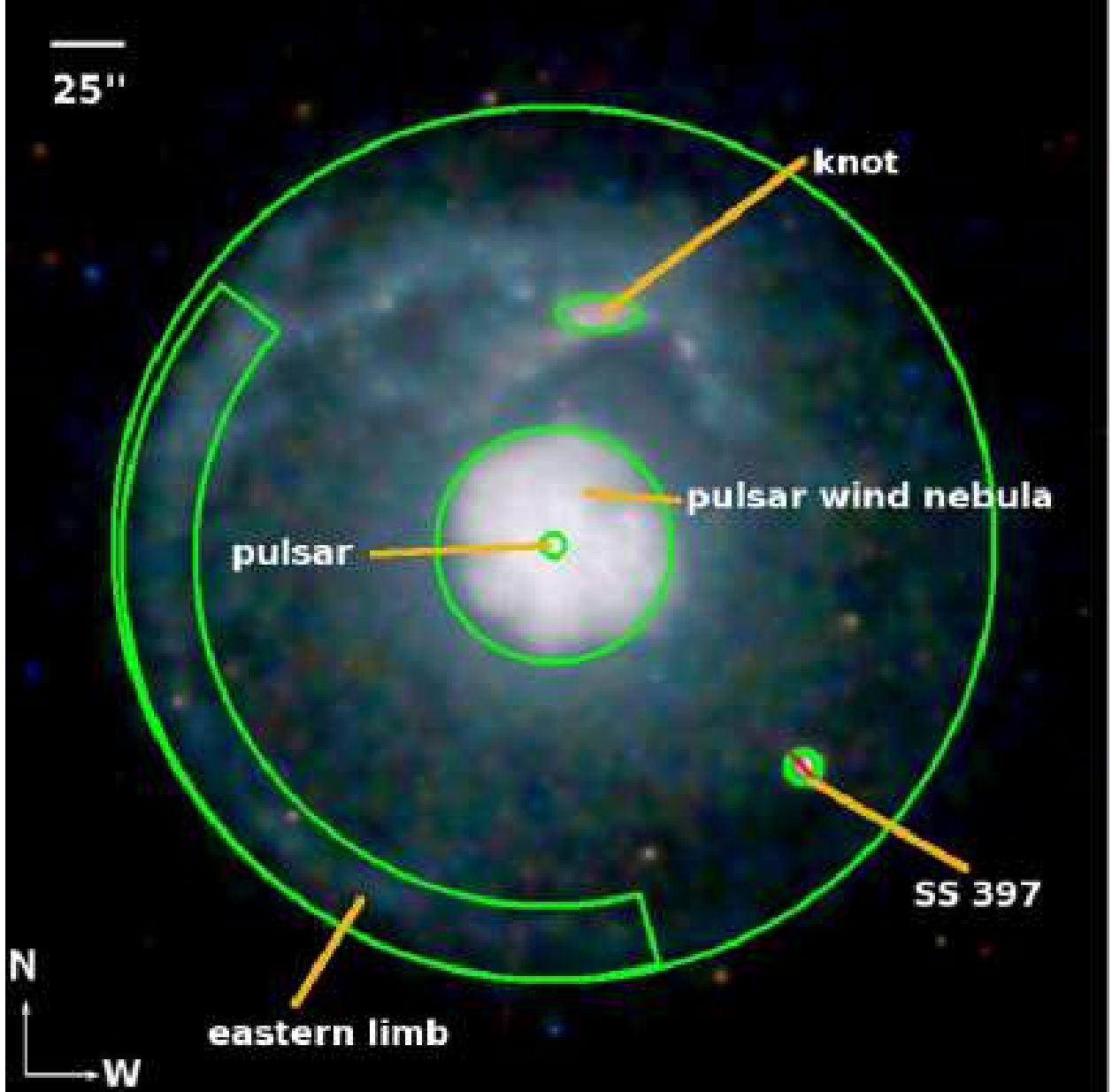


Fig. 1.— Regions used in the spectral analysis of G21.5–0.9, with the northern knot and eastern limb highlighted. The point source SS 397 was excluded from the data prior to extracting spectra. The image is $377'' \times 377''$ and is centred on the location of the X-ray peak ($\alpha(2000) = 18^{\text{h}}33^{\text{m}}33^{\text{s}}.54$, $\delta(2000) = -10^{\circ}34'07''.6$), which is the pulsar location. At a distance of 5 kpc, the PWN of G21.5–0.9 has a diameter of 1.9 pc and the halo has a diameter of 7.3 pc. Adapted from Matheson & Safi-Harb (2005).

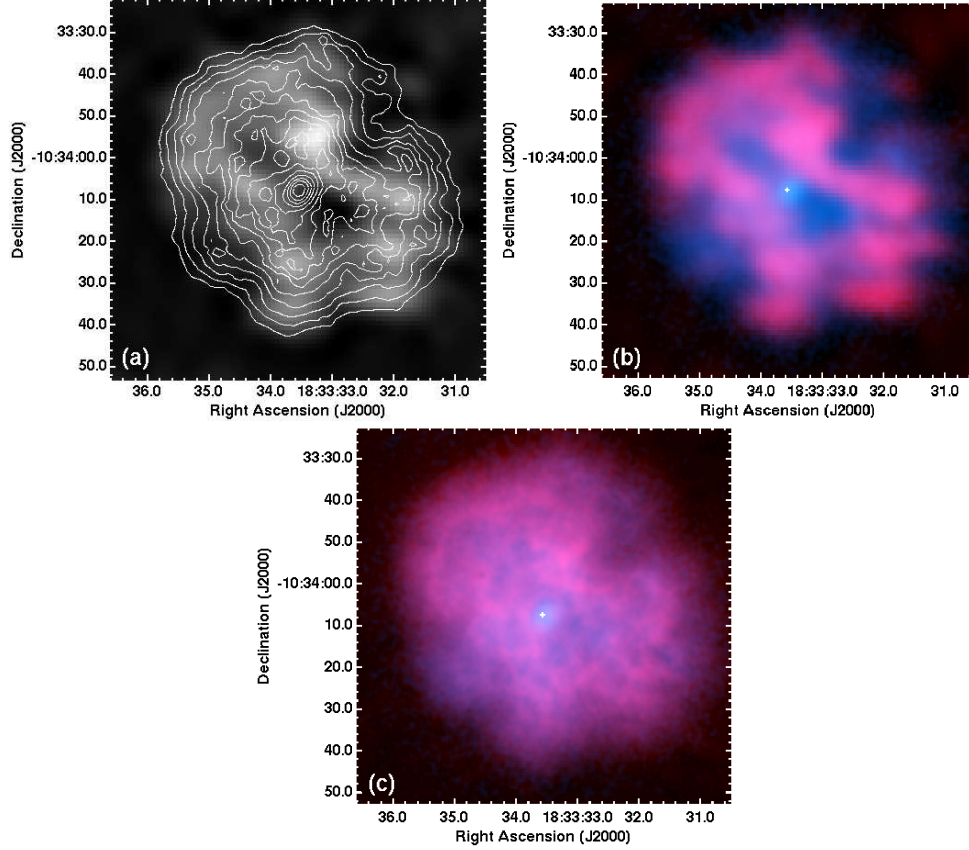


Fig. 2.— (a) 22.3 GHz radio data from the Nobeyama Millimeter-Wave Array (resolution $8''$, Fürst et al. 1988), overlaid with *Chandra* ACIS X-ray (0.2–10.0 keV) contours. Both the X-ray and radio data are in a log scale. (b) The 22.3 GHz radio data are here shown in red and overlaid with the 0.2–10.0 keV X-ray data shown in blue. The cross indicates the position of PSR J1833–1034. (c) 4.75 GHz radio data from the VLA (see Bietenholz & Bartel (2008) for details) coloured in red overlaid with the 0.2–10.0 keV X-ray data (again coloured in blue). The FWHM of the radio beam was $0.82'' \times 0.53''$ at p.a. 10° . See §2.1 for details.

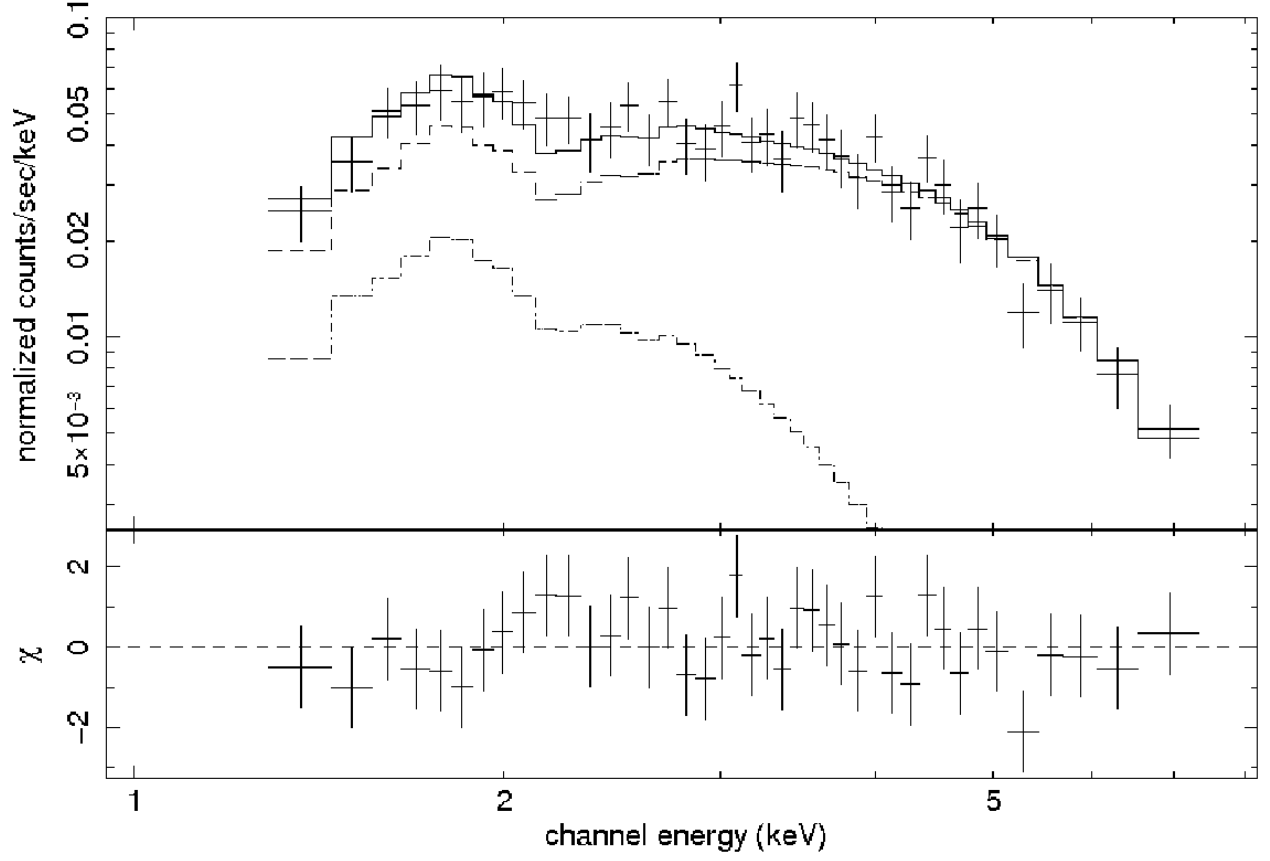


Fig. 3.— Sample spectrum (obsID 6071) of the pulsar PSR J1833–1034, showing the data (crosses), model (solid line), *power* and *bbody* components (dashed lines), and residuals (bottom panel) of the fit to an absorbed power-law + blackbody ($wabs*(power+bbody)$ in *XSPEC*).

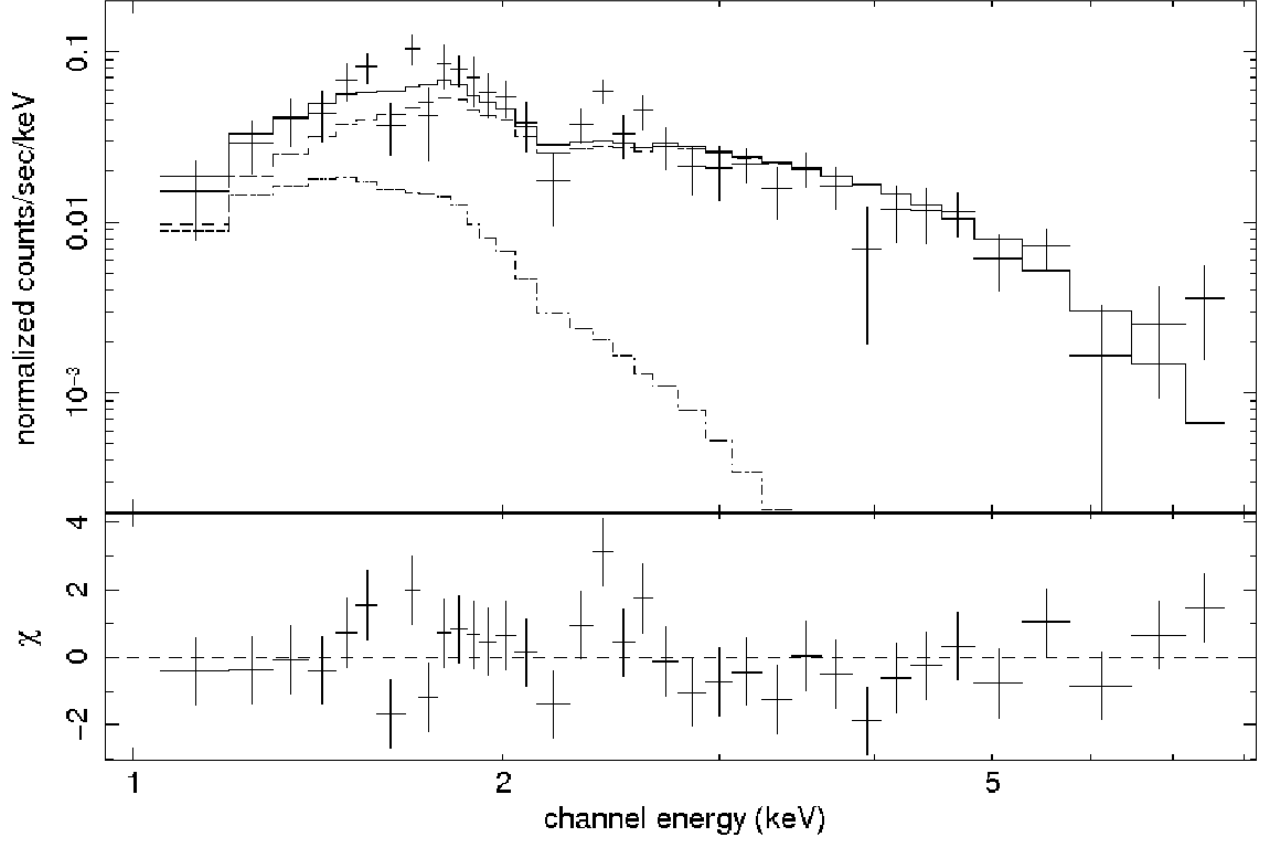


Fig. 4.— Sample spectrum (obsID 6071) of the southern half of the X-ray halo ($r = 40''$ - $153''$), showing the data (crosses), model (solid line), model components (dotted lines), and residuals (bottom panel) of the fit to an absorbed power-law + pshock model with $N_{\text{H}} = 2.24 \times 10^{22} \text{ cm}^{-2}$ (*wabs*(power+pshock)* in *XSPEC*).

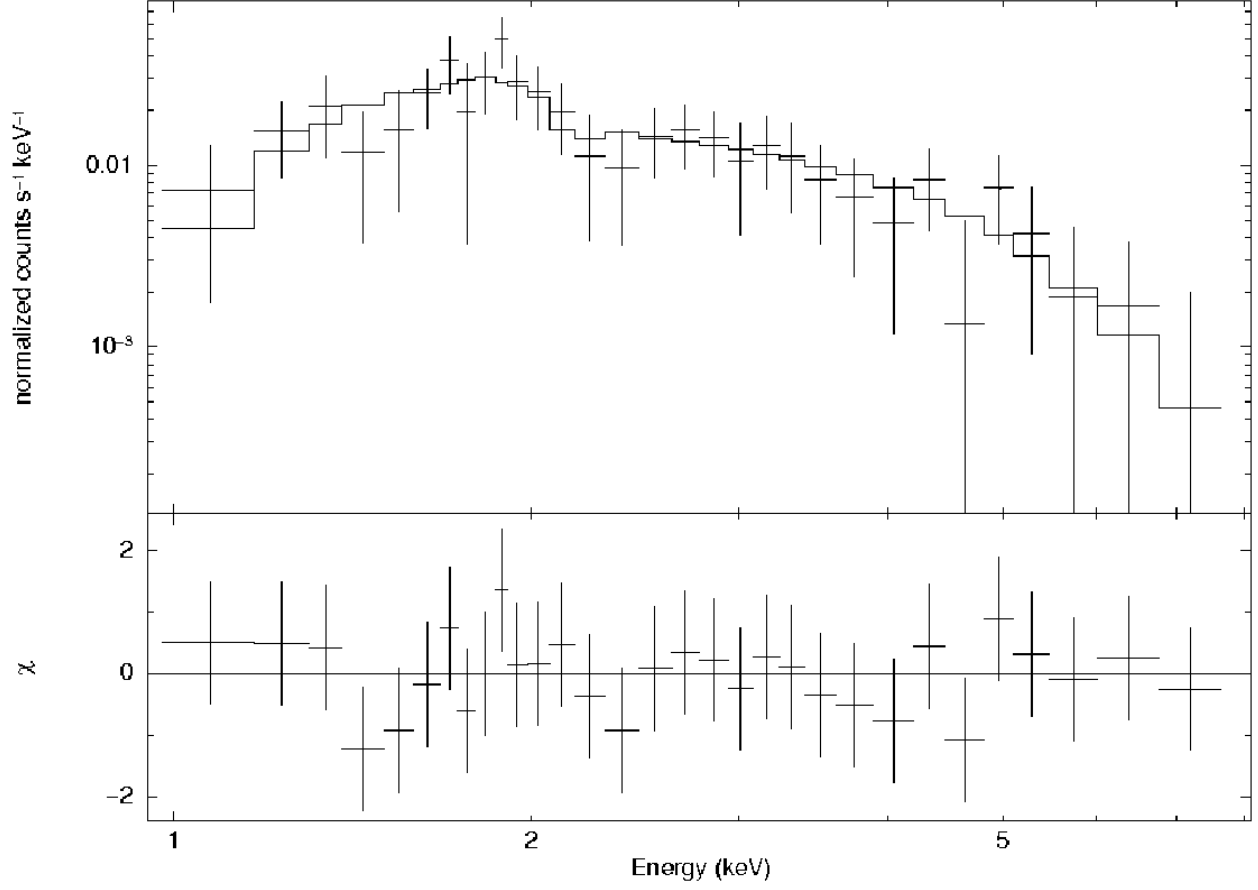


Fig. 5.— Sample spectrum (obsID 6071) of the eastern limb, showing the data (crosses), model (solid line), and residuals (bottom panel) of the fit to an absorbed srcut model with $N_{\text{H}} = 2.24 \times 10^{22} \text{ cm}^{-2}$ and $\alpha = 0.5$ (*wabs*srcut* in *XSPEC*).

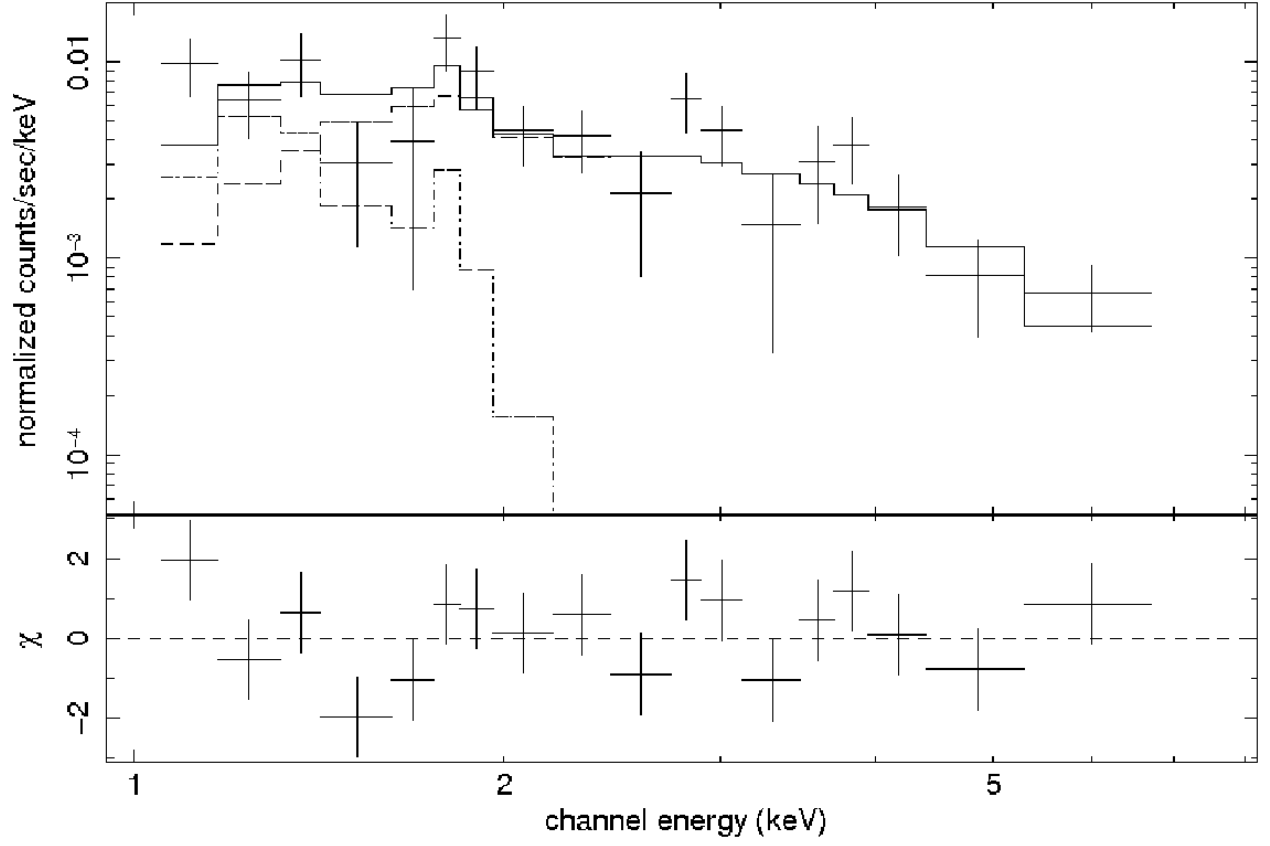


Fig. 6.— Sample spectrum (obsID 6071) of the brightest northern knot, showing the data (crosses), model (solid line), and residuals (bottom panel) of the fit to an absorbed power-law + pshock model with $N_{\text{H}} = 2.24 \times 10^{22} \text{ cm}^{-2}$ (*wabs*(power+pshock)* in *XSPEC*).

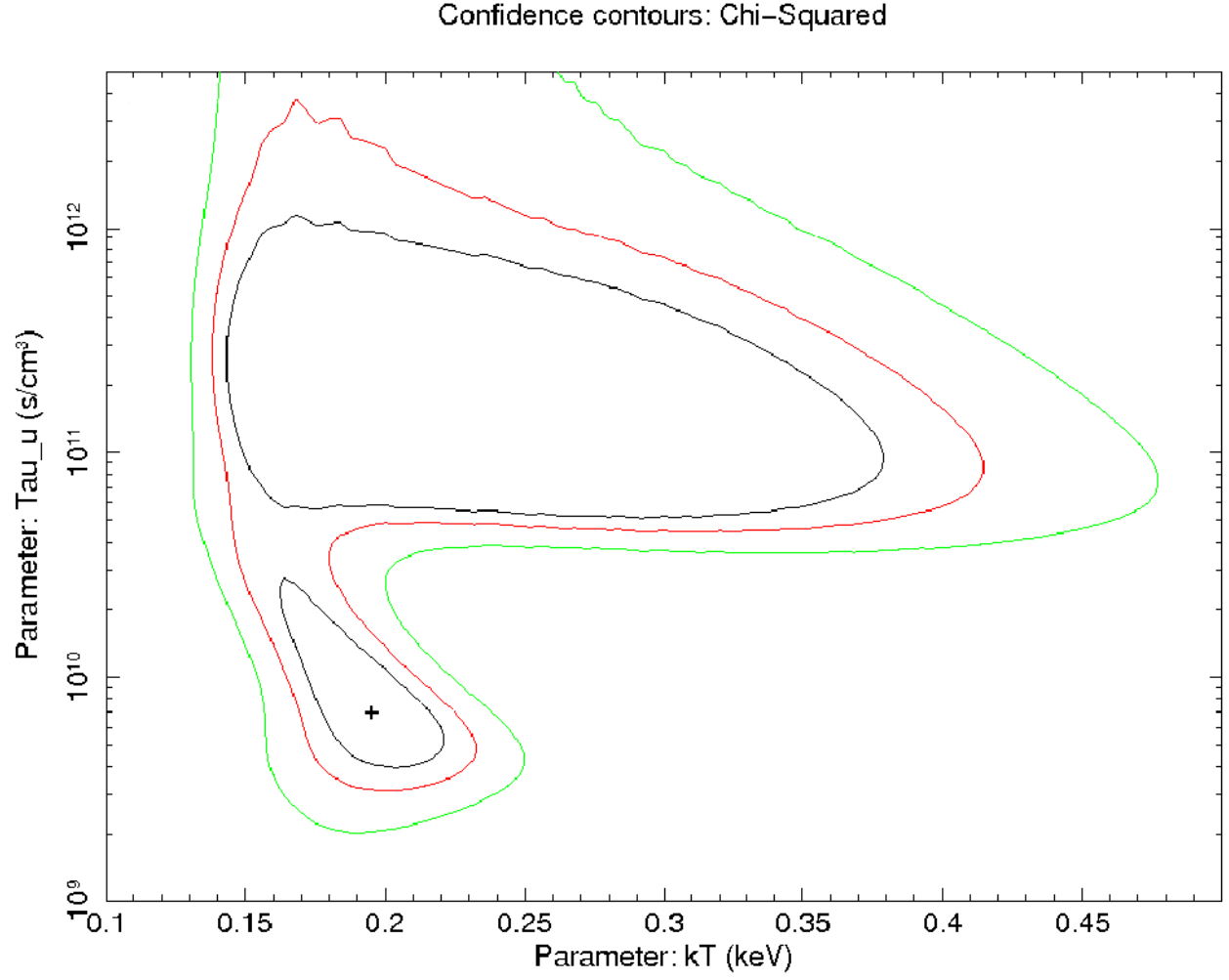


Fig. 7.— n_{et} and kT confidence contours for the *power+pshock* fit to the brightest knot north of the PWN.

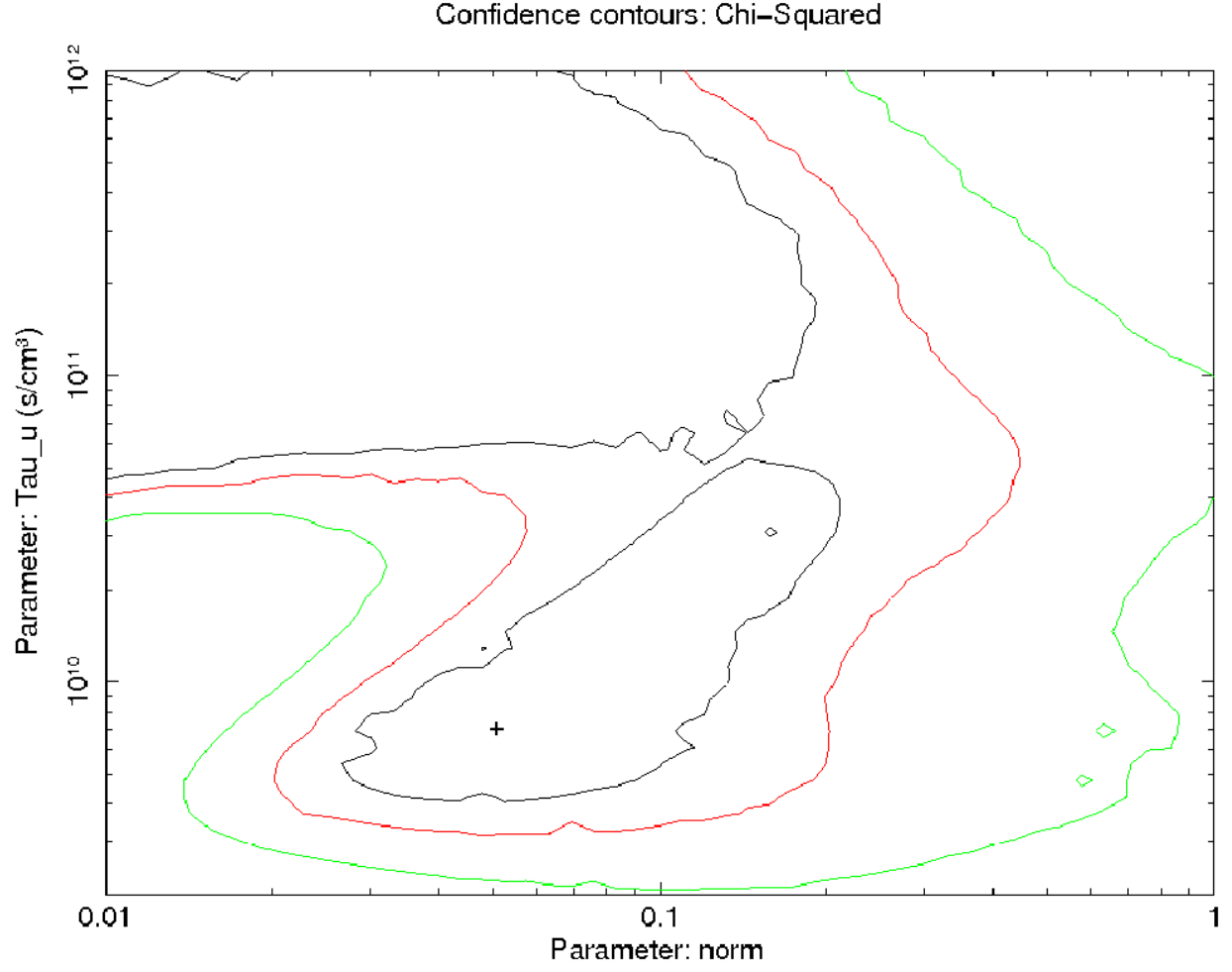


Fig. 8.— Emission measure and kT confidence contours for the *power+pshock* fit to the brightest knot north of the PWN.

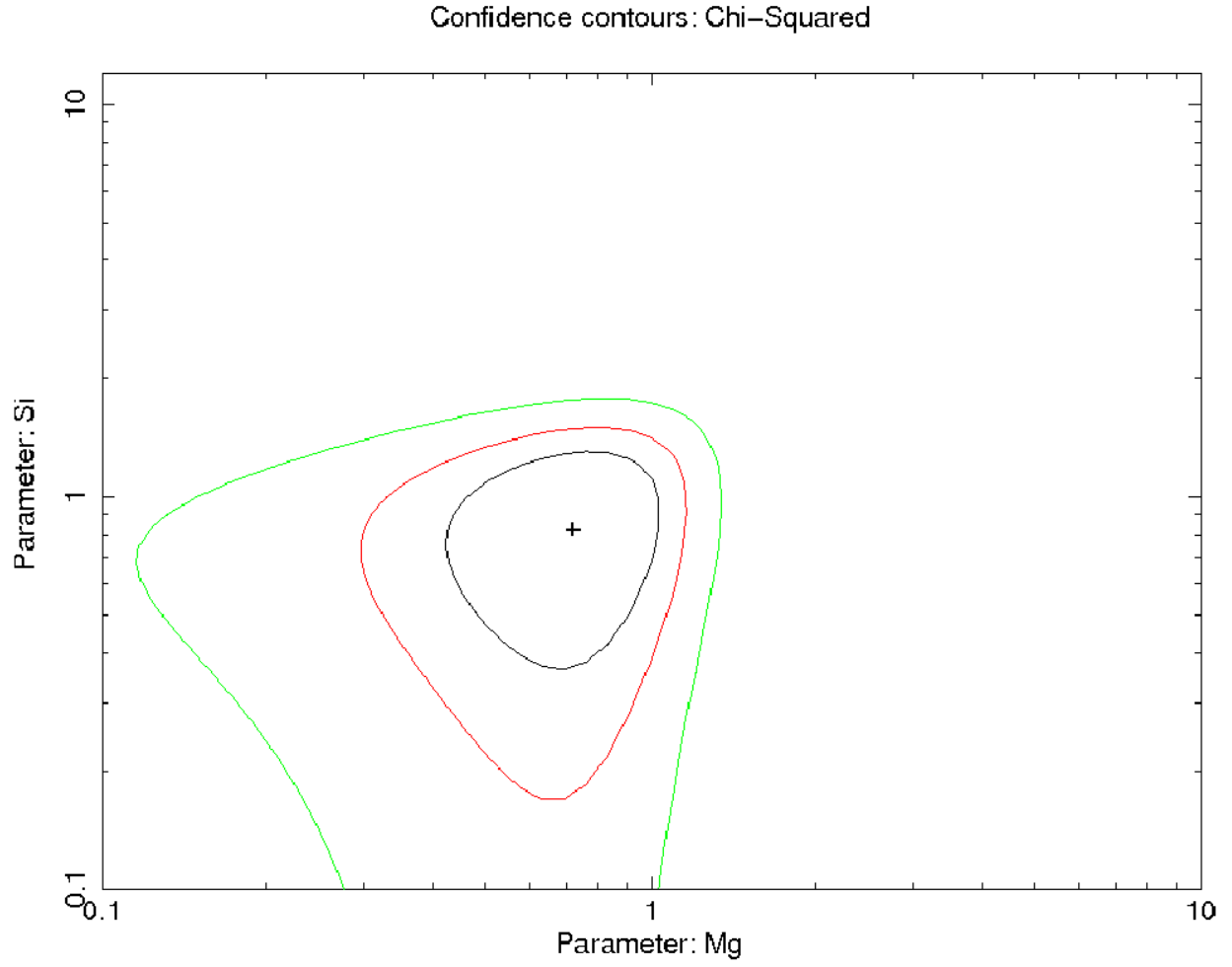


Fig. 9.— Elemental abundances in the brightest knot to the north of the PWN. The axes range shown is the same as that of Bocchino et al. (2005).

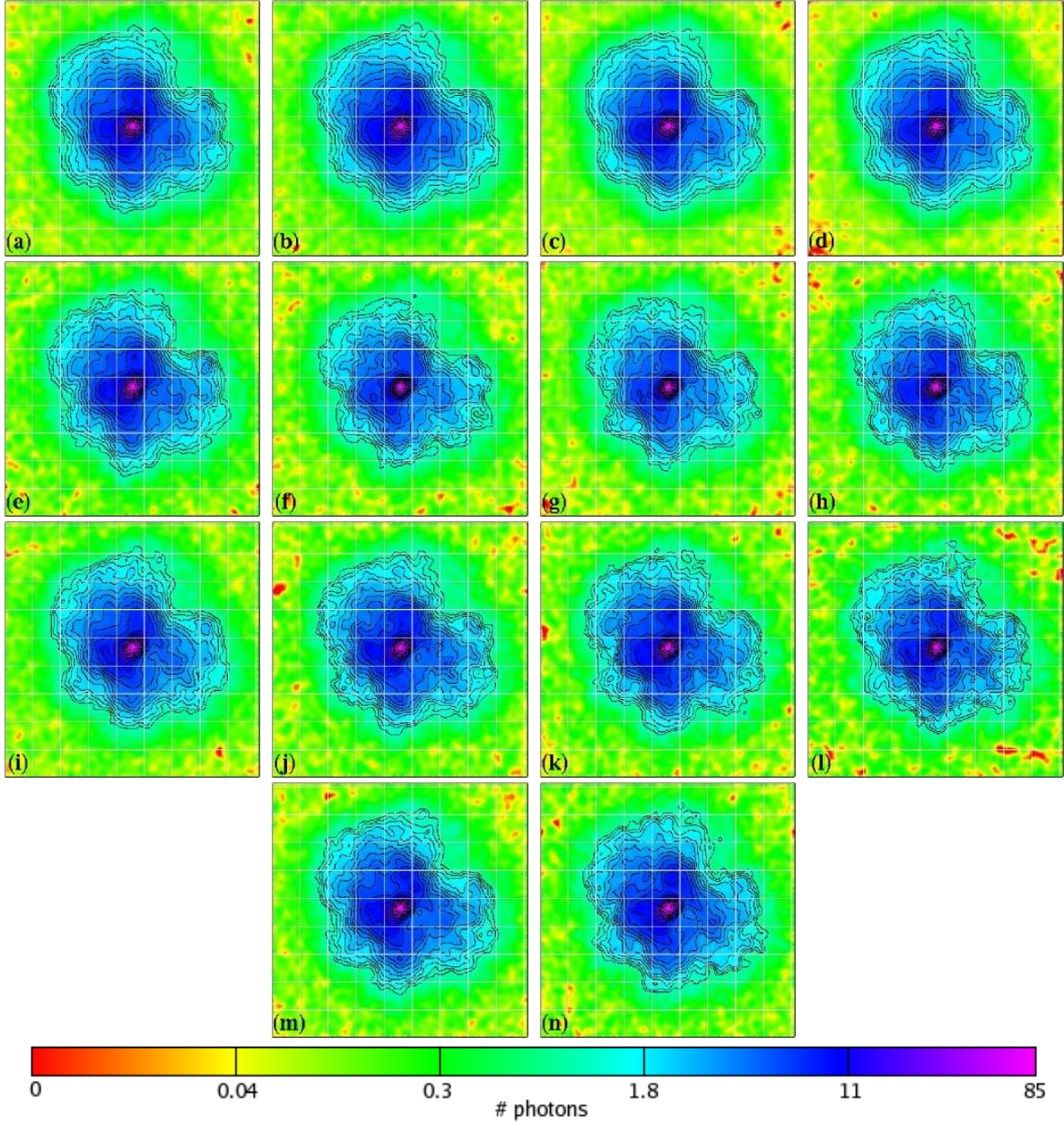


Fig. 10.— Combined ACIS images of G21.5–0.9 for each observing date. All images are normalized to an effective exposure of 20 ks. The colourbar used is a logarithmic scale and identical in all images. Contours are at 1, 1.26, 1.60, 2.02, 2.55, 3.22, 4.07, 5.14, 6.49, 8.20, 10.36, 13.09, 16.54, 20.90, 26.40, 33.36, 42.15, 53.25, 67.28, and 85 photons per pixel. Each image is $90''$ on a side. These images form the frames of a movie in the online version of the journal. (a) 1999-08 (b) 1999-11 (c) 2000-05 (d) 2000-07 (e) 2000-09 (f) 2001-03 (g) 2001-07 (h) 2002-09 (i) 2003-05 (j) 2003-11 (k) 2004-03 (l) 2004-10 (m) 2005-02 (n) 2006-02.

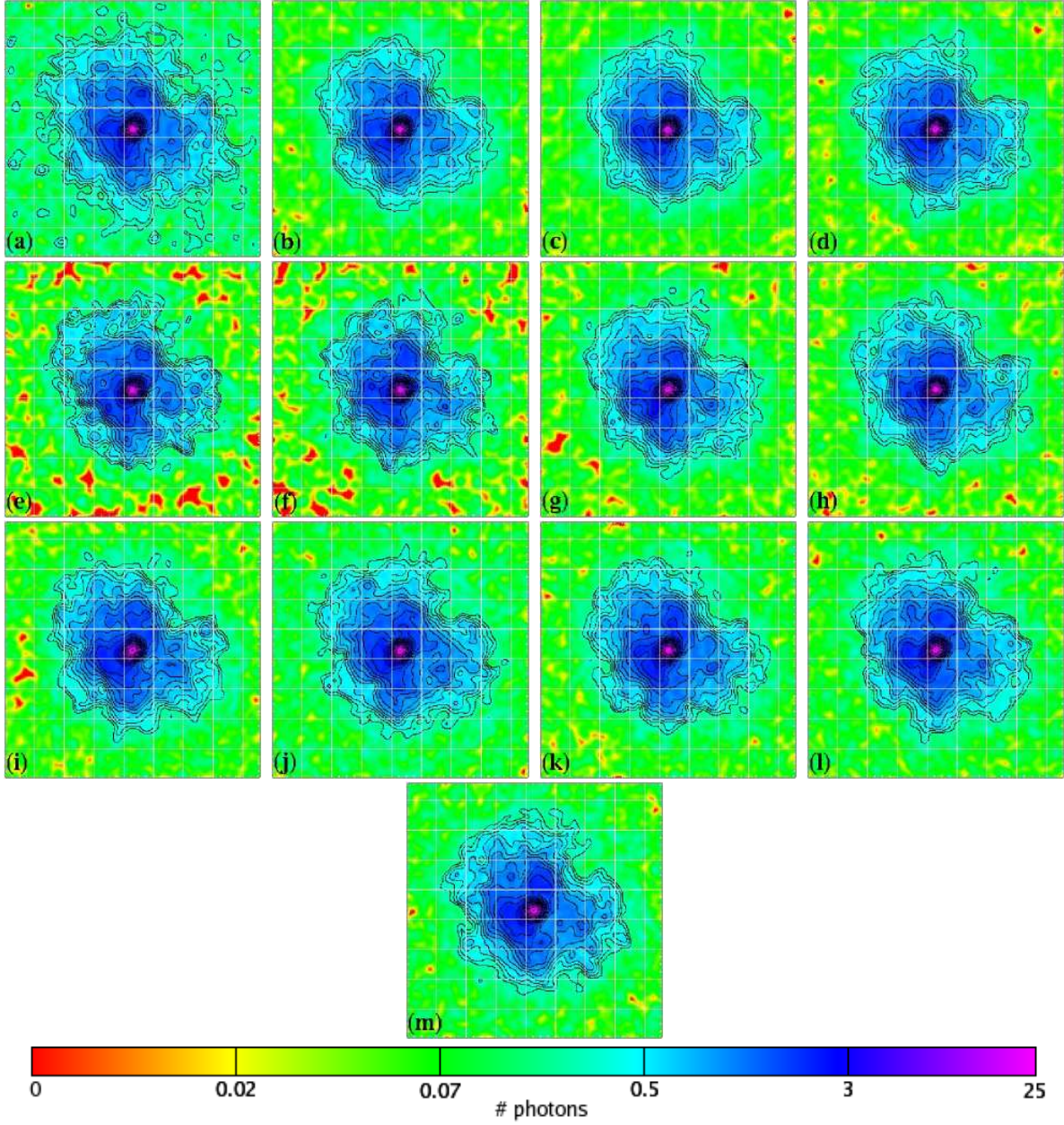


Fig. 11.— Combined HRC-I images of G21.5–0.9 for each observing date. All images are normalized to an effective exposure of 20 ks. The colourbar used is a logarithmic scale and identical in all images. Contours are at 0.3, 0.38, 0.48, 0.60, 0.76, 0.96, 1.21, 1.53, 1.93, 2.43, 3.08, 3.88, 4.90, 6.19, 7.81, 9.85, 12.44, 15.69, 19.81, and 25 photons per pixel. Each image is $90''$ on a side. These images form the frames of a movie in the online version of the journal. (a) 1999-09 (b) 1999-10 (c) 2000-02 (d) 2000-09 (e) 2001-03 (f) 2001-07 (g) 2002-03 (h) 2002-07 (i) 2003-05 (j) 2003-11 (k) 2004-03 (l) 2005-02 (m) 2006-02.

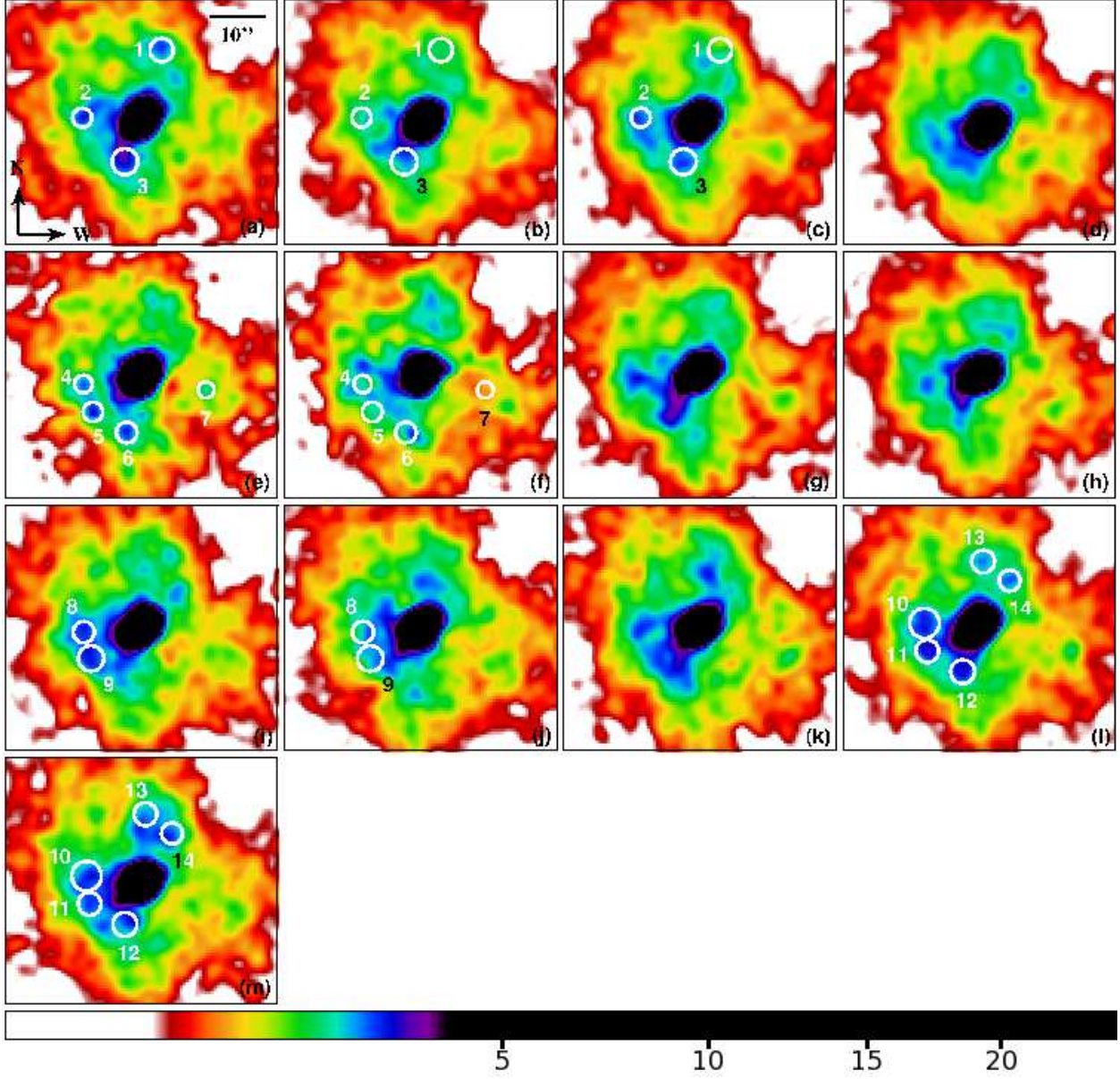


Fig. 12.— Variability in the PWN G21.5–0.9. HRC-I images from the dates (a) 1999-09 (b) 1999-10 (c) 2000-02 (d) 2000-09 (e) 2001-03 (f) 2001-07 (g) 2002-03 (h) 2002-07 (i) 2003-05 (j) 2003-11 (k) 2004-03 (l) 2005-02 (m) 2006-02. The numbered circles mark the location of some knots of emission which either move or fade by the next image in the sequence. See Section 4 for details.

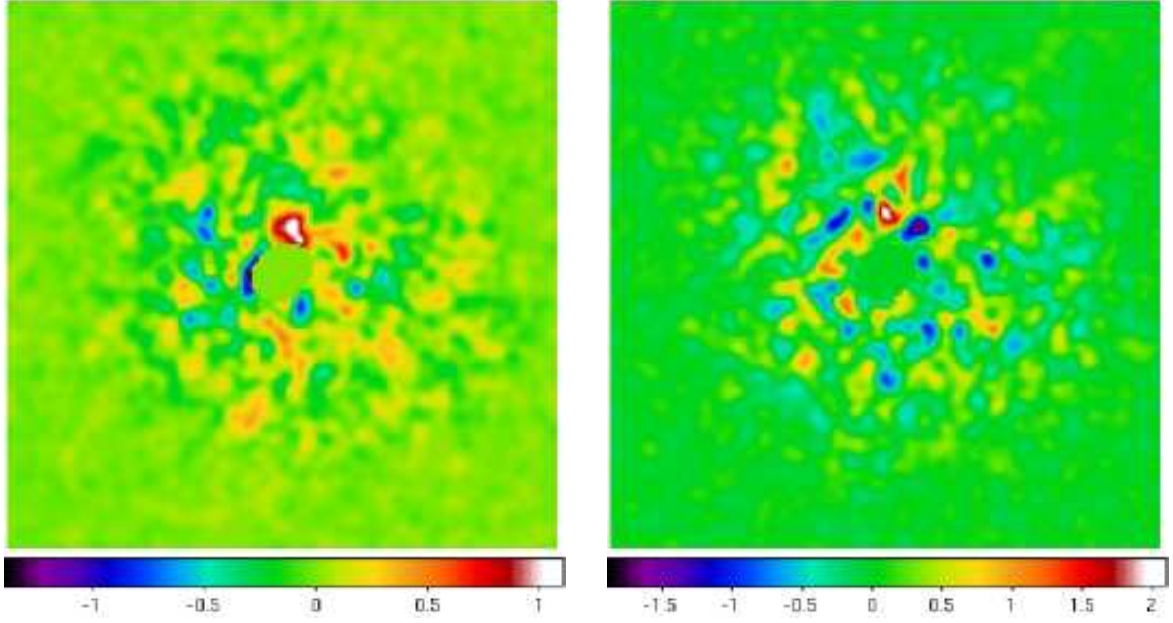


Fig. 13.— Sample difference images created by subtracting one of the images in Figure 10 from the following image in the sequence. The emission near the pulsar was omitted to highlight the variability in the PWN. White and red indicate regions that are brighter in the later image. Black, purple, and blue indicate regions that are brighter in the earlier image. Colourbars are in units of counts per pixel. (a) 2000-07 minus 2000-05 (b) 2006-02 minus 2005-02.

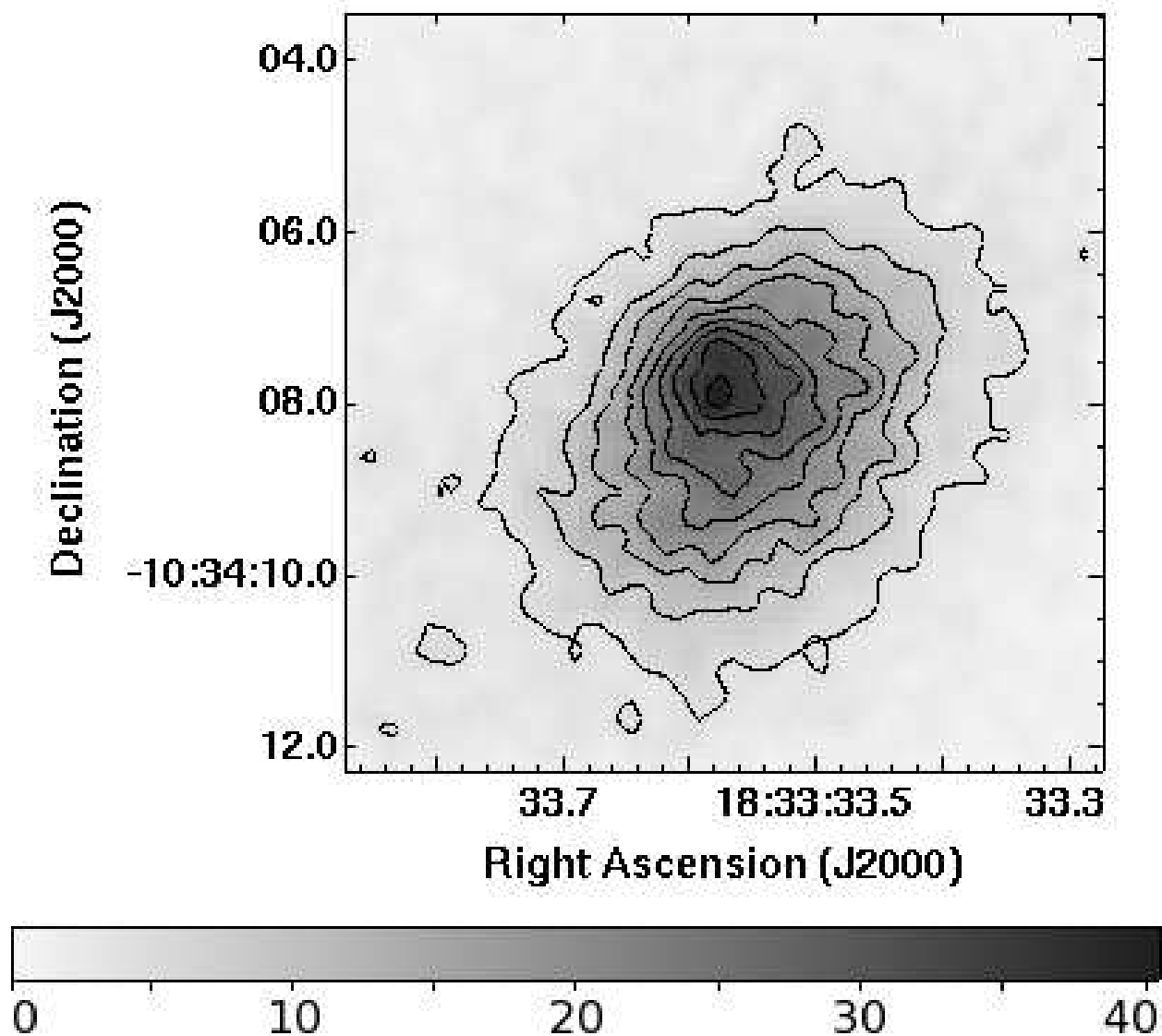


Fig. 14.— HRC-I image of the central emission of G21.5–0.9 (smoothed by 2 pixels). The pulsar appears offset to the northeast. The image is 9'' across. Contours are linearly spaced at 4.3, 8.6, 12.8, 17.1, 21.4, 25.7, 29.9, 34.2, and 38.5 counts per pixel.